

Phenylalanine in the Gas Phase – The Impact of Side-Chain Fluorination

Master Thesis
by
Rayoon Chang

Submitted to the Department of Biology, Chemistry and Pharmacy
of the Freie Universität Berlin
May 02, 2018–Nov 05, 2018



The work presented in this thesis was performed from May 02, 2018 to Nov 05, 2018 in cooperation between the groups of Prof. Dr. Kevin Pagel at the Institute of Chemistry and Biochemistry of the Freie Universität Berlin and Prof. Dr. Gert von Helden at the Department of Molecular Physics of the Fritz Haber Institute of the Max Planck Society.

First Examiner: Prof. Dr. Kevin Pagel
Freie Universität Berlin

Second Examiner: Prof. Dr. Beate Koksch
Freie Universität Berlin

Date of Defense: Nov 26, 2018

Acknowledgments

Foremost, I would like to express my sincere gratitude to my chief examiner Prof. Dr. Kevin Pagel, for providing me the opportunity to write my bachelor thesis back in 2016 and welcoming me back to write my master thesis. I would also like to thank Prof. Dr. Gert von Helden and Prof. Dr. Gerard Meijer for providing me, as a guest, the opportunity to conduct experiments at the super-effective iMob at the Fritz Haber Institute. I would also like to thank Prof. Dr. Beate Kokschi for being my second examiner without any hesitations. I cannot thank Dr. Waldemar Hoffmann enough, for his exceptional guidance and the invaluable advices, and also for understanding whatever I said with my broken language. To Prof. Dr. Gert von Helden and Daniel A. Thomas, Ph.D. am I very thankful for the support regarding the theoretical calculations. As a very beginner in this field, I would not have been able to conduct the simulations myself without their kind assistance. I would like to acknowledge Christian Manz, Eike Mucha, and Dr. Waldemar Hoffmann for taking their time to proof-read my thesis. I am gratefully indebted to them for their valuable comments on this thesis. Very special thanks are dedicated to my amazing office buddies – Christian Manz and Dr. Waldemar Hoffmann. Thank you for always listening to me, entertaining, encouraging and supporting me no matter what. I would like to thank the members of AG Pagel and AG von Helden, not to forget the whole MP department, for the heart-warming welcome. I always felt at home and had a lot of fun, especially at the Christmas party and the summer festival we organized, fun game nights, crazy birthday and graduation parties, and hope for much more to come. Special thanks are dedicated to my lovely Balkans. Without you guys, my master studies would have been very dry and colorless. Thank you for always being by my side, and also for making me into a perfect Balkan – who is always late. But do not forget, στα αγγλικά παρακαλώ.

Last but not least, I would like to express my very profound gratitude to my beloved parents and my brother for their unconditional love and unfailing support. I am happy that we could spend the last four years together in Germany and am very excited to experience what is in line.

Abstract

Aggregation and misfolding proteins can occur by the interplay of various intra- and intermolecular interactions and such phenomenon can be the hallmark of various diseases, such as Alzheimer's disease and type II diabetes. Within the main amino acid (AA) building blocks, phenylalanine (Phe) is suspected to play a crucial role in such aggregation-related diseases due to the unique property of its hydrophobic, aromatic side-chain. Phe is also known to self-assemble into fibrillar structures in solution and in the gas phase. To modulate such aggregation propensity, H/F substitution of AA side-chains is commonly used. Recent investigations show that H/F substitution not only induces a change in electronic properties, but also introduces new interactions, such as hydrogen bonding or electrostatic interactions. Especially, C–F \cdots H interaction is known to have about 25% of the strength of a typical hydrogen bond and detection of such weak interactions is often challenging by condensed-phase techniques. The “clean-room” environment of the gas phase, on the other hand, enables investigation of isolated systems free from any solvent interactions and is thus ideal in studying such weak interactions. Utilizing ion mobility-mass spectrometry (IM-MS), the size and shape of ions can be probed in the gas phase. IM-MS can also serve as a pre-selection tool to perform size- and conformer-selective gas-phase infrared multiple photon dissociation (IRMPD) spectroscopy. Gas-phase IR spectroscopy delivers intrinsic molecular properties and enables an effective comparison to *ab initio* calculations. Within this work, the influence of side-chain fluorination of Phe on its self-assembly propensity is studied as a model system of aggregating species in the gas phase. The results show that side-chain fluorination of protonated Phe results in attractive C–F \cdots H interaction between the protonated amine and the neighboring fluorine substituent on the *ortho*-position of the phenyl ring. This results in a red-shift of the C–F stretching mode in the IRMPD spectrum and highly depends on the site of fluorination. Additionally, the data show that the AA self-assembly is initiated by the formation of a homodimer. Perfluorination of the side-chain significantly reduces the electron density of the aromatic ring due to the electron-withdrawing nature of fluorine substituents. Thus, the assembly of side-chain perfluorinated Phe into larger clusters is strongly suppressed due to the absence of the attractive cation- π interaction, whereas the side-chain monofluorinated Phe derivatives are still capable of forming clusters of various sizes and charge states. This example highlights the importance of understanding initial key interactions within AA dimers which is not only crucial in predicting the aggregation propensity of larger AA clusters but may even be applied to larger systems such as small peptides to unravel their implication on peptide and protein aggregation.

Contents

1	Introduction	1
2	Fundamentals	2
2.1	Amino Acids	2
2.2	Amino Acid Clusters in the Gas Phase.....	3
2.3	Fluorination of Amino Acids	5
2.4	Ion Mobility-Mass Spectrometry	6
2.4.1	Fundamentals	6
2.4.2	Collision Cross-Section Calculation.....	8
2.5	Infrared Spectroscopy	9
2.5.1	Fundamentals	9
2.5.2	Infrared Multiple Photon Dissociation Spectroscopy.....	10
2.5.3	IR Spectroscopy of Amino Acids	11
3	Instrument and Data Acquisition	13
3.1	Experimental Details	13
3.1.1	Ion Mobility-Mass Spectrometry.....	13
3.1.2	Infrared Multiple Photon Dissociation (IRMPD) Spectroscopy.....	14
3.1.3	Data Acquisition and Analysis.....	14
3.1.4	Sample Preparation.....	14
3.2	Computational Methods	15
4	Results and Discussions	16
4.1	Aggregation Propensity	16
4.1.1	Phenylalanine.....	16
4.1.2	Side-Chain Monofluorination	18
4.1.3	Side-Chain Perfluorination.....	20

4.2 Monomers.....	21
4.2.1 Phenylalanine	21
4.2.2 Side-Chain Monofluorinated Phenylalanine Isomers	23
4.2.3 Pentafluorophenylalanine.....	27
4.3 Dimers	29
4.3.1 Phenylalanine	29
4.3.2 Side-Chain Monofluorinated Phenylalanine Isomers	30
4.3.3 Pentafluorophenylalanine.....	41
5 Conclusion and Outlook	45
6 References	47
Appendix A	51
Appendix B	53
Appendix C	60
Statutory Declaration	63

1 Introduction

Protein misfolding and aggregation are hallmarks of various diseases such as Alzheimer's disease, Huntington's disease and type II diabetes.¹⁻³ The aggregation of the involved proteins is often triggered by a central hydrophobic core in which the hydrophobic amino acid (AA) phenylalanine (Phe) is frequently observed. A promising strategy to modulate the folding and aggregation properties of peptides and proteins is the H/F substitution of the AA side-chains, in particular Phe to pentafluorophenylalanine (F₅-Phe).⁴ This can not only suppress critical aromatic interactions by reducing the electron density of the π -system,⁵ but also introduces steric repulsion⁶ and can therefore alter the assembly pathway to non-specific, and non-toxic protein oligomers. However, H/F substitutions not only influence the electronic property and hydrophobicity of the medium, but can also introduce new interactions, such as C-F \cdots H hydrogen bonding or electrostatic interactions, which can yield a complementary effect and provide additional stability to toxic folding intermediates.⁷⁻⁸ Predicting the impact of H/F substitution on the aggregation process of peptides and proteins is therefore very challenging. Previous studies showed that F₅-Phe substitution can, depending on the system, lead to both enhancement as well as suppression of the aggregation tendency.⁹⁻¹⁰ Most importantly, the interplay of numerous non-covalent interactions such as hydrogen bonding, electrostatic, hydrophobic and π - π interactions complicates the identification of the key aspects behind the aggregation propensity.

Within this work, the self-assembly of protonated Phe and the impact of side-chain monofluorination (*ortho*-, *meta*- and *para*-fluorophenylalanine), and perfluorination (F₅-Phe) is studied on different structural levels utilizing size- and shape-sensitive ion mobility-mass spectrometry (IM-MS), intra- and intermolecular vibration-sensitive gas-phase infrared (IR) spectroscopy and atomically resolved *ab initio* calculations. IR spectroscopy and theoretical calculations are used for structural elucidation of critical interactions within the protonated monomer and dimer structures, whereas IM-MS is used to derive information on the respective AA cluster distribution and aggregation propensity.

2 Fundamentals

2.1 Amino Acids

The 21 proteinogenic AAs consist of an amine and a carboxylic acid functional group. They are also defined as α -AAs due to the amine bonded to the α -carbon relative to the carboxyl group. As shown in Figure 2.1, the α -carbon is a stereocenter (except for glycine due to two indistinguishable hydrogen atoms) and two chiral enantiomeric forms are present for each α -AA, with the “left-handed” L-stereoisomer found predominantly in nature.¹¹



Figure 2.1 Scheme of L- and D- stereoisomers of α -AA with side-chain R.

The AAs have different side-chains R with different physical and chemical properties, affecting the interaction with the environment, even when they assemble themselves into larger peptides and proteins. In an aqueous solution with a neutral pH value, the carboxylic acid functional group (COOH) of the amino acid can be easily deprotonated to become a negatively charged carboxylate (O⁻C-O⁻). In contrast, the amino group (NH₂) can be easily protonated to become a positively charged ammonium group (NH₃⁺). Therefore, most amino acids are typically present as zwitterionic species when in an aqueous solution. But once they are isolated in the gas phase, non-zwitterionic (canonically neutral) forms are known to be energetically favored.^{12,13} Interestingly, in the presence of an ion, the zwitterionic structure of the AA can be stabilized through additional interactions, such as hydrogen bonding and electrostatic interactions.¹³ The general non-zwitterionic and zwitterionic states of L-amino acid are depicted in Figure 2.2.



Figure 2.2 Scheme of L-amino acid with side-chain R, in non-zwitterionic (also referred to as the canonically neutral structure, left) and zwitterionic (right) structure.

2.2 Amino Acid Clusters in the Gas Phase

AA are known to self-assemble into clusters of various sizes and charges when brought into the gas phase upon electrospray-ionization (ESI).¹⁴ Clusters of AAs can be considered as model systems to study the key aspects that govern aggregation tendencies in peptides and proteins. Based on data from ion mobility-mass spectrometry (IM-MS), Do et al. have for example developed an empirical model for the peptide aggregation propensity based on the growth trends of various AA clusters.¹⁵ Nonetheless, only few studies focused on predicting the self-assembly trend of peptides and proteins with AA model systems so far. Most studied have rather focused on the structural characterization of specific AA dimers and/or higher clusters.¹⁶⁻²¹ Previous studies show that structural characterization of protonated AA monomers by gas-phase IR spectroscopy enables to distinguish between possible non-zwitterionic and zwitterionic structures by observing the characteristic band positions of their functional groups.²² The assembly of AA monomers can be driven by series of non-covalent interactions, such as hydrogen bonding and π -interactions, or *via* ionic interactions, in the presence of charge carriers. Previous experimental and theoretical efforts indicate that the formation of protonated AA dimers occurs mainly *via* hydrogen bonding between amine and/or carboxyl functional groups, which can be assigned to three types of interactions, as visualized in Figure 2.3.²¹

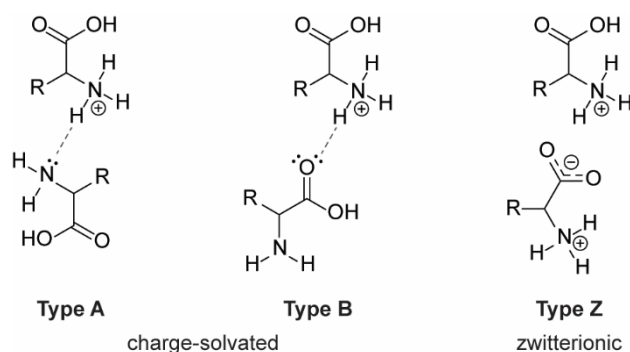


Figure 2.3 Possible pairwise interaction motifs of protonated amino acid (AA) homodimers, where R is the side-chain of the respective AA. In all three types of interaction, one of the two AAs carries the positive charge on the amine due to protonation. In type A interaction, a protonated amine of one AA interacts with a neutral amine of the second charge-solvated AA. Type B interaction is stabilized by an attractive interaction between a protonated amine and a neutral carboxyl group of the other charge-solvated AA. Type Z interaction contains a protonated amine interacting with the deprotonated carboxylate of the second AA of zwitterionic state.

In AA dimers, with one of the two AA building blocks carrying the positive charge on the amine group, the other counterpart can be present in a charge-solvated (non-zwitterionic)

or zwitterionic form. Of the two possible charge-solvated interactions, type A structures are stabilized by hydrogen bonding between two amine groups ($-\text{NH}^+\cdots\text{NH}_2-$), which is usually observed in cases where the AA side-chain provides additional charge-stabilization as seen by protonated homodimers of phenylalanine, serine, tryptophan and tyrosine.^{17, 20-21} In cases of alanine, cysteine, isoleucine and valine, where the side-chain is not actively involved in charge-stabilization type B interaction is observed to be more preferred.^{18, 21, 23} In this case, the dimer is preferably formed through the interaction of a protonated amine with a neutral carboxylic acid ($-\text{NH}^+\cdots\text{O}=\text{COH}-$). Type Z interactions are formed between a protonated amine with a deprotonated carboxylate of the zwitterionic counterpart ($-\text{NH}^+\cdots\text{OCO}-$) and two of the rare examples are the protonated homodimers of proline and glycine.²⁴⁻²⁵

These results indicate that the structure of protonated AA monomers and the type of interaction within the AA homodimers are strongly influenced by the characteristics of their respective side-chains. As a model system, the self-assembly property and the structure of resulting monomers and homodimers of phenylalanine will be studied. The effect of side-chain will be further investigated by side-chain monofluorination and perfluorination.

2.3 Fluorination of Amino Acids

Fluorine has emerged as the key element in medicinal chemistry for its unique properties. For example, fluorine-containing compounds are widely used in pharmaceutical industry, materials science and many other fields, due to their unique advantages regarding metabolic stability, biocompatibility, change of biophysical properties, binding affinity and many more.⁴ Moreover, H/F substitution of α -L-AAAs is nowadays commonly used to modulate properties of peptides and proteins.²⁶⁻²⁸ Within α -AAAs, Phe is one of the most studied systems due to the properties associated with its hydrophobic, aromatic side-chain in relation to biological systems. Phe is known to self-assemble into fibrillar structures in the condensed phase and also in the gas phase.²⁹⁻³² Previous studies indicate that the fibrillar aggregate is stabilized by various intermolecular hydrogen bonds as well as aromatic π - π interactions.³¹ Also, the interaction of Phe is suspected to play a crucial role in protein aggregation-related diseases, such as phenylketonuria.³²⁻³³ To modulate its aggregation propensity and interaction properties, H/F substitution of the side-chain was conducted in various systems to study the influence of electron withdrawing groups to cation- π interactions.

Due to the broad field of application and its great potential, a better understanding of fluorine-specific interactions is of ongoing interest.³⁴⁻³⁵ However, the fluorine-specific interactions are very weak, usually about 25% of the strength of a typical hydrogen bond,³⁵ and if embedded within a large molecular system, their detection in solution is often difficult. Previous crystallographic studies suggest that for attractive C-F \cdots H interaction to occur, an internuclear distance shorter than the sum of the van der Waals radii ($r_{\text{vdW}}(\text{H}) + r_{\text{vdW}}(\text{F}) < 2.67 \text{ \AA}$, with $r_{\text{vdW}}(\text{H}) = 1.20 \text{ \AA}$ and $r_{\text{vdW}}(\text{F}) = 1.47 \text{ \AA}$) is necessary.³⁵⁻³⁷ It is also controversially discussed, whether the C-F \cdots H interactions can be classified as hydrogen bonds, or rather as electrostatic or dipole interactions. The “clean room” environment of the gas phase, on the other hand, makes it possible to gain fundamental knowledge about intra- and intermolecular interactions of molecules and molecular aggregates. A promising method to conduct such studies are the orthogonal gas phase techniques ion mobility-mass spectrometry (IM-MS) and gas phase infrared (IR) spectroscopy.³⁸⁻⁴¹ This method enables the characterization of selected species in the presence of many others. Since solvent effects are excluded in the gas-phase, very weak interactions are not obscured as in the condensed phase and can therefore be detected. The absence of solvent-interactions also enables effective comparison between the gas-phase IR spectra and *ab-initio* calculations.⁴²

2.4 Ion Mobility-Mass Spectrometry

2.4.1 Fundamentals

The combination of ion mobility spectrometry (IMS) and mass spectrometry (MS) is a very powerful method to investigate AAs in the gas phase. Whereas MS enables the separation or isolation of molecular ions by their mass-to-charge ratio (m/z), ion mobility spectrometry (IMS) enables the separation and differentiation of ions based on their size, shape and charge.⁴³⁻⁴⁴ To investigate AAs by the orthogonal method of ion mobility-mass spectrometry (IM-MS), however, they have to be transferred from solution into the gas phase in forms of charged species. From the various methods of generating ions (e.g. electrospray ionization (ESI),^{14, 45} matrix-assisted laser desorption (MALDI),⁴⁶ sublimation⁴⁷ and many more), a soft ionization technique, called *nano*-electrospray ionization (*n*-ESI), is used within this work to generate AA ions with various sizes and charges.^{14, 48-49}

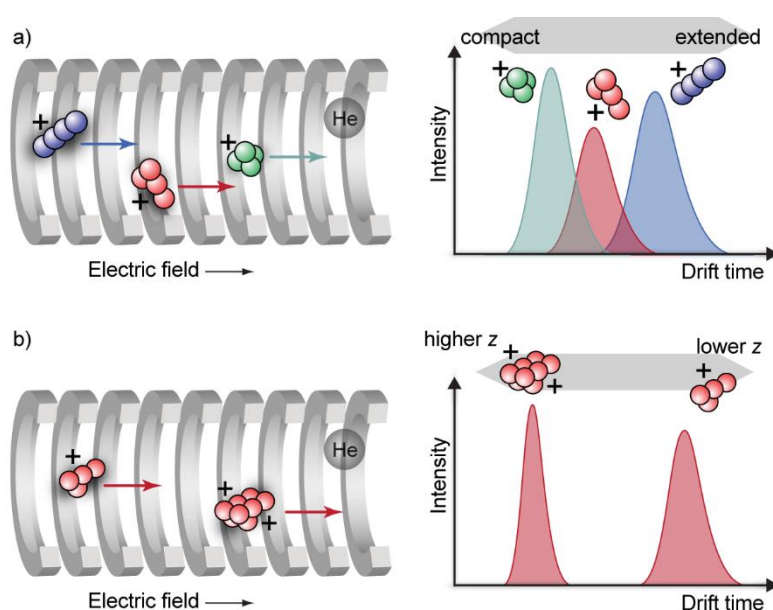


Figure 2.4 Schematic representation of mobility of injected ions (a) with the same m/z ratio, resulting in different drift times due to their difference in shape. The ion with a more compact size (green) results in a shorter drift time than the extended ion (blue), since it undergoes fewer collisions with the buffer gas in the IM cell. (b) Ions with the same m/z ratio are separated according to their charge. The drift time of the ions is depicted as an arrival time distribution (ATD).

Upon injection of these ions into a linear IM cell filled with an inert buffer gas (e.g. N_2 , He or Ar), they traverse through the IM cell under the influence of an applied weak electric field. During their migration, the ions undergo collisions with the buffer gas, where more

extended ions (blue) experience more collisions with the buffer gas than the compact ions (green) and are thus retained. This results in a longer drift time, as presented in Figure 2.4 (a). Ions of higher charge states on the other hand, have higher mobility due to the greater influence of the electric field and therefore exit the IM cell at a shorter drift time (Figure 2.4 (b)).⁴⁴

The drift time (t_D) is classified as the time an ion requires to travel through an IM cell of length L at a constant temperature (T), pressure (p) and applied drift voltage (U). Hereby, the velocity of the ion (v_D) is constant and can be expressed as a product of the ions mobility (K) and the electric field (E):

$$v_D = \frac{L}{t_D} = KE = \frac{KU}{L} \quad (1)$$

where the experimentally obtained drift time (t_{exp}), is the sum of t_D and the time an ion spends outside of the IM cell until it reaches the detector. Thus, the time offset (t_0) also needs to be taken into consideration:

$$t_{exp} = t_D + t_0 = \frac{L}{KE} + t_0 = \frac{L^2}{KU} + t_0 \quad (2)$$

2.4.2 Collision Cross-Section Calculation

The t_D depends on various instrumental parameters such as the L , applied E , p and T inside the IM cell. Therefore, it is advantageous to convert t_D to an instrument-independent, universally comparable parameter, namely the collision cross-section (CCS, Ω). To calculate the CCS value (Ω), the mobility of the ion (K) has to be determined from the experimentally determined t_D using equation 2.

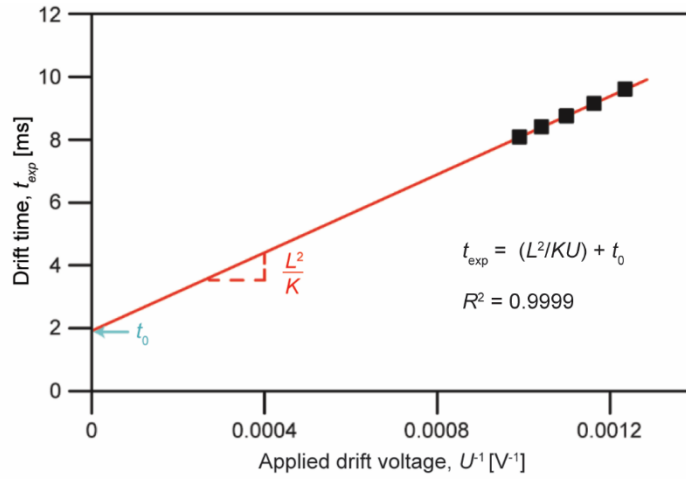


Figure 2.5 The experimental drift time (t_{exp}) is plotted as a function of the inversed drift voltage U^{-1} . The resulting linear regression follows equation 2 and allows to extract K from the slope.

As shown in equation 2, t_{exp} is inversely proportional to K and U . Hence, by varying the applied U , a linear regression can be obtained, as shown in Figure 2.5. The slope is equal to L^2/K and the intercept of this fit corresponds to t_0 . At known values of K , p and T , the CCS value (Ω) can be determined by using the Mason-Schamp equation.⁵⁰

$$\Omega = \frac{3q}{16N} \sqrt{\frac{2\pi}{\mu k_B T} \frac{1}{K} \frac{p_0}{p} \frac{T}{T_0}} \quad (3)$$

Here, q is the total charge of the ion ($q = ez$), N the number density of the buffer gas, μ the reduced mass of ion-buffer gas molecule system, k_B the Boltzmann constant, p_0 the standard pressure and T_0 the standard temperature.

2.5 Infrared Spectroscopy

2.5.1 Fundamentals

The molecular bonds are non-rigid and can engage in various movements. The motion of a molecule can be classified as translational, rotational and vibrational terms. A molecule with N number of atoms has in total $3N$ degrees of freedom, of which the vibrational motion accounts for $3N-6$ terms ($3N-5$ for linear molecules). Each vibration of a molecule is unique to the type of the oscillators and their local environments – thus delivers detailed information regarding the type of functional groups within the molecule and also regarding the non-covalent interactions, (such as hydrogen bonding and electrostatic interactions). Such information is embedded within the spectrum in the form of absorption bands, with varying relative band positions and intensities. Infrared (IR) spectroscopy is a widely used method for structural determination of unknown species. An IR-absorption occurs when the irradiated light is in resonance with the molecular vibration, e.g. induces a change in the dipole moment.

2.5.2 Infrared Multiple Photon Dissociation Spectroscopy

Classical IR spectroscopy is based on absorption spectroscopy, where the attenuation of light is measured upon interaction with a medium. The following Lambert Beer law describes this phenomenon as follows:

$$I_{\nu} = I_0 \cdot e^{-\sigma_{\nu}ln} \quad (4)$$

where I_{ν} and I_0 are the intensities of light before and after it passes through the path length l of the sample with number density of n and absorption cross section of σ_{ν} . For gaseous ions however, the limited ionic density to a space charge limit of $\sim 10^6$ ions per cm^3 is insufficient to attenuate the incoming light for absorption experiments.⁵¹ Therefore, action spectroscopy is used to obtain gas-phase spectra of ions, where the influence of light on the ion is monitored. Similar to the Lambert-Beer law, the number of ions influenced by the light (N_{ν}) can be expressed as follows:

$$N_{\nu} = N_0 e^{-\sigma_{\nu}\Phi_{\nu}} \quad (5)$$

where N_0 is the number of ions before the irradiation of the light and Φ_{ν} the photon flux. This method requires high photon flux, which can be realized by infrared multiple photon dissociation spectroscopy (IRMPD) utilizing the free electron laser (FEL) as a powerful light source. In IRMPD spectroscopy, the fragmentation of the investigated ions is measured by the sequential absorption of multiple resonant photons. The energy from each absorbed photon is distributed over the entire molecule *via* intramolecular vibrational redistribution (IVR). The molecule can therefore repeatedly absorb multiple photons until the internal energy of the system gradually exceeds the dissociation threshold. Due to the IVR process, the dissociation of the molecule occurs through the fragmentation of the weakest bond, which are usually the non-covalent bonds in the case of biomolecular complexes.

2.5.3 IR Spectroscopy of Amino Acids

The functional groups of AAs deliver characteristic vibrational bands in the mid-IR region (depicted in Figure 2.5) from which information regarding the fine-structure of the molecule can be deduced.⁵²

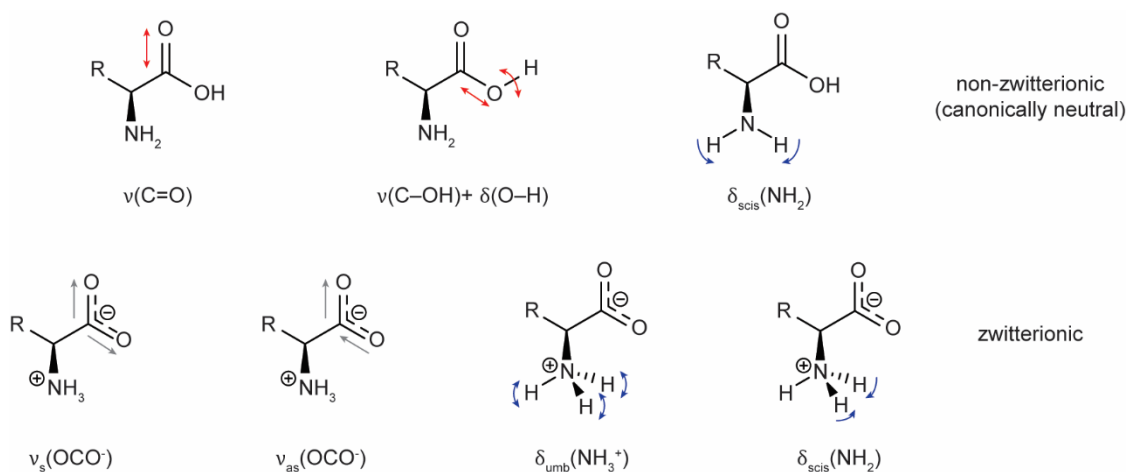


Figure 2.5 Characteristic mid-IR vibrational modes of non-zwitterionic (top) and zwitterionic AAs (bottom).

One of the diagnostic IR features of AAs in the fingerprint region is the C=O stretch mode of neutral carboxylic acids, $\nu(\text{C}=\text{O})$, which is usually observed between $1600\text{--}1800\text{ cm}^{-1}$.²² The other are the symmetric and antisymmetric stretching modes of deprotonated carboxylates, $\nu(\text{O}-\text{C}-\text{O}^-)$, where a weak symmetric O-C-O⁻ vibration occurs at $1300\text{--}1400\text{ cm}^{-1}$ along with a stronger antisymmetric O-C-O⁻ vibration at $1600\text{--}1650\text{ cm}^{-1}$.⁵³ In addition, the C-F stretch mode, $\nu(\text{C}-\text{F})$, is also of interest due to the fluorinated Phe analogues that will be studied within this thesis. The $\nu(\text{C}-\text{F})$ mode is expected in the range of $1200\text{--}1300\text{ cm}^{-1}$.⁵⁴

The vibrational modes of AAs are highly sensitive towards the hydrogen bonding networks. Upon association in hydrogen bonding, the vibrational frequency (ν) of a molecular bond can increase or decrease, depending on the type of the functional group. The vibrational frequency (ν) can be expressed by the following equation:

$$\nu = \frac{1}{2\pi} \sqrt{\frac{D}{\mu}} \quad (6)$$

where D is the bond strength and μ the reduced mass ($m_1 \cdot m_2 / (m_1 + m_2)$). If the carboxyl functional group (C=O) engages in hydrogen bonding, the bond strength is weakened and the $\nu(\text{C}=\text{O})$

mode shifts to lower wavenumbers (also referred to as a red-shift). However, if the hydroxyl (O–H) or the amine (NH₂ or NH₃⁺) functional groups or the hydrogen atoms of the amino group participate in hydrogen bonding, the C–O bond and the N–H bond are strengthened, and through the contraction of the affected bonds, a blue-shift occurs (increase in wavenumber) for the bending modes.⁵⁵⁻⁵⁶ Therefore, it is possible to analyze the intra- and intermolecular arrangements of a molecule based on the vibrational signature of the functional groups.

3 Instrument and Data Acquisition

3.1 Experimental Details

3.1.1 Ion Mobility-Mass Spectrometry

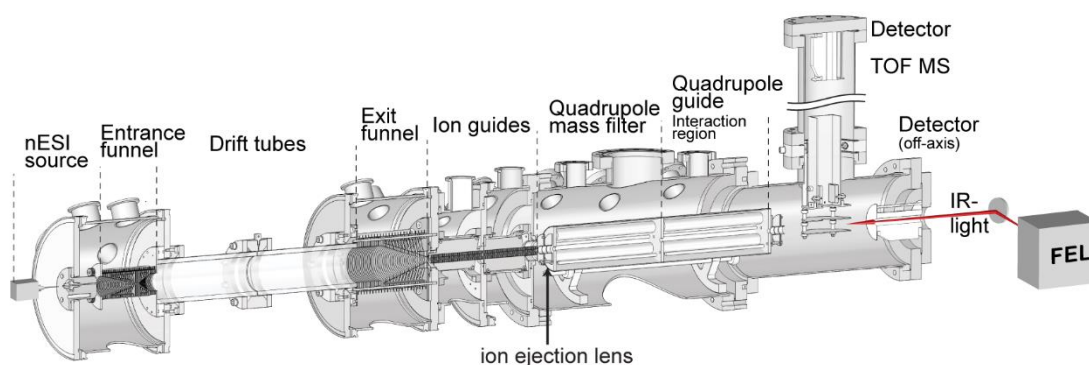


Figure 3.1 Technical drawing of home-built drift-tube (DT) mass spectrometer: The instrument consists of a *nano*-electrospray ionization (*n*ESI) source, funnel for guiding ions into the different regions of the spectrometer, linear ion mobility (IM) drift tube, quadrupole mass filters for m/z -selection as well as for interaction with the Fritz Haber Institute free electron laser (FHI-FEL) and a time-of-flight (TOF) mass analyzer.⁵⁷⁻⁵⁸

A home-built hybrid drift-tube ion mobility-mass spectrometer connected to the Fritz Haber Institute-Free Electron Laser (FHI-FEL) has been used to perform the experiments presented within this thesis.⁵⁷⁻⁵⁸ A simplified representation of the instrument is depicted in Figure 3.1. Briefly, $\sim 5 \mu\text{L}$ of sample is loaded into in-house prepared Pd/Pt-coated borosilicate capillaries and *nano*-electrosprayed by applying 0.6–0.8 kV. The generated ions are then trapped over several tens of milliseconds and pulsed from a radio frequency (RF) operating ion (entrance) funnel, and subsequently pulsed into a linear drift tube (80.55 cm) filled with ~ 4 mbar helium buffer gas where ions are guided by a weak electric field ($10\text{--}15 \text{ V cm}^{-1}$). As the ions traverse through the drift cell, more extended ions collide with the buffer gas atoms more frequently and therefore require longer time to exit the drift cell. Higher charged ions on the other hand exit the drift cell much faster and thus experience a shorter drift time. After exiting the ion mobility cell, ions are radially confined by a second RF operating exit funnel and guided by ring electrodes into the high vacuum region of the instrument (10^{-8} mbar). An electrostatic einzel lens focuses the ions into the quadrupole mass filter, where they are selected based on their mass-to-charge ratio (m/z). The arrival time distribution (ATD) is obtained by recording the time-dependent ion current of the m/z -selected species after release from the ion trap by an electron multiplier

detector. Therefore, this method enables the separation and identification of ions based on the difference in mass, charge, size and shape.⁵⁹ The ion's drift time can be further converted to an instrumentally independent rotationally-averaged collision cross-section (CCS) using the Mason-Schamp equation (Equation 4).⁵⁰ Otherwise, to obtain the mass spectra, ions can be deflected and pulsed into the Wiley-McLaren type time-of-flight (TOF) mass spectrometer, equipped with an electron multiplier detector.

3.1.2 Infrared Multiple Photon Dissociation (IRMPD) Spectroscopy

Electrostatic gating utilizing an einzel lens prior to mass-selection by the quadrupole mass filter allows the selection of ions of a narrow drift time window (80–200 μ s). The drift time- and m/z -selected ions are irradiated with the intense and narrow-bandwidth IR light of the FHI-FEL in the interaction region of the instrument (second quadrupole). When IR light is resonant with the molecular vibration, it leads to the absorption of multiple photons followed by dissociation of the molecule. Monitoring the dissociation yield as a function of the wavelength by the TOF mass analyzer yields a highly reproducible infrared multiple photon dissociation (IRMPD) spectrum of drift time- and m/z -selected ions. The final IR spectrum is produced by averaging over two runs, in which the IRMPD spectra are obtained by measuring 30 scans every three wavenumber steps in the range of 1000–1900 cm^{-1} .

3.1.3 Data Acquisition and Analysis

The linear DT ion mobility-mass spectrometer is controlled by a LabVIEW-based software by which mass spectra, arrival-time distributions (ATDs) and gas-phase IRMPD spectra were measured. Manual data analysis was performed by means of OriginPro 2016 (OriginLab, Northampton, MA). Adobe Illustrator CC 2015 (Adobe Systems GmbH, Munich, Germany) was used to prepare the Figures.

3.1.4 Sample Preparation

The enantiopure L-isomer of phenylalanine (Phe) was purchased from Sigma-Aldrich (Taufkirchen, Germany) and the enantiopure, L-forms of fluorinated phenylalanine derivatives (*ortho*-, *meta*- and *para*-fluorophenylalanine (*o*F-Phe, *m*F-Phe, *p*F-Phe respectively) and pentafluorophenylalanine (F₅-Phe)), from TCI Deutschland GmbH (Eschborn, Germany), and dissolved in pure water without further purification to yield a final concentration of 5 mM.

3.2 Computational Methods

Within this work, theoretical calculation is used to study the structure of protonated monomers and dimers of Phe and its fluorinated derivatives. The starting geometries are prepared by conformational search simulation as implemented in MACROMODEL⁶⁰ tool of Maestro Suite (*Schrödinger*) program, using the OPLS3 force field.⁶¹ Each simulation generated 7–15 structures for individual monomers which were further optimized using density functional theory (DFT). In the case of protonated dimers, the starting geometries are prepared according to the three interaction types of A, B and Z (Figure 2.3). From the 100–300 structures generated for every dimer (within an energy window of 40 kJ mol⁻¹), structures within a 20 kJ mol⁻¹ window of the global minimum were further optimized by DFT. Within the DFT calculation, geometry optimization and harmonic frequency calculations were performed as implemented in the Gaussian 16 program⁶² at the B3LYP level of theory, using the aug-cc-pVDZ basis set and adding empirical dispersion corrections using the Grimme D3 method⁶³ with ultrafine integration grids. The vibrational modes are scaled by 0.971⁶⁴ and convoluted with Gaussian functions with a full width at half-maximum of 0.5% to fit the experimental spectra. The molecular vibrations were visualized and analyzed on the Gauss View platform.⁶⁵ Averaged over three calculations, theoretical CCS (TMCCS_{He}) values of the optimized structures are calculated using the MOBCAL⁶⁶⁻⁶⁷ program using the trajectory method and helium as buffer gas at 298 K.

4 Results and Discussions

4.1 Aggregation Propensity

4.1.1 Phenylalanine

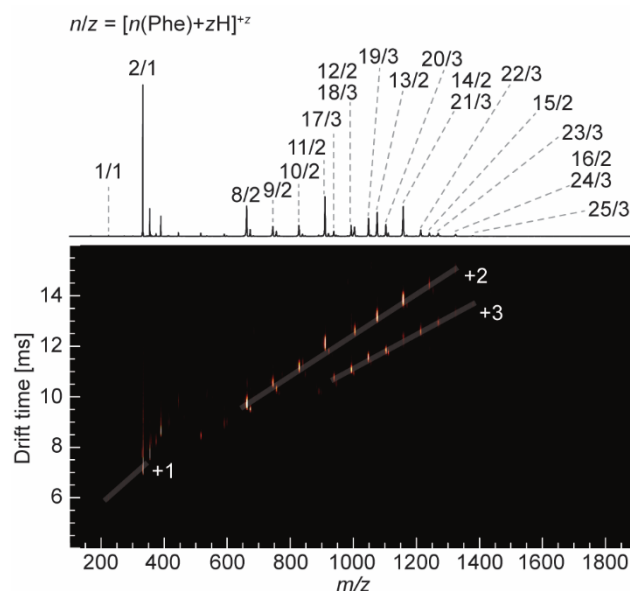


Figure 4.1 TOF mass spectrum of protonated phenylalanine (top) and the corresponding drift time versus m/z plot (bottom). Individual clusters are labelled with n/z where n corresponds the number of Phe monomers in the cluster and z the charge state. The singly, doubly and triply protonated clusters follow distinct growth trends and are marked with white lines in the drift time scans.

To effectively study the influence of side chain fluorination, a reference is necessary. Therefore, the basic model system phenylalanine (Phe) is first studied to better understand the intrinsic properties of basic building blocks (monomers and presumably dimers) that govern the aggregation propensity. First, the self-assembly propensity of Phe is studied by IM-MS. Figure 4.1 shows the TOF mass spectrum (top) and two-dimensional drift time scan (bottom) of protonated Phe upon *nano*-electrospray ionization (*n*-ESI) of 5 mM enantiopure, aqueous solution. The observed species are labelled with n/z in the mass spectrum, where n corresponds to the number of amino acid (AA) monomers and z the charge state of the cluster. Single peaks in the mass spectrum may consist of clusters with different masses and charges, but the same m/z value. The assignment of each m/z peak was therefore aided by the drift time scan in which the cluster growth trend of different charge states can be followed easily, as marked with white lines (Figure 4.1, bottom). In addition, experimental $^{DT}CCS_{He}$ values were also determined. At different instrumental settings, the signal intensity of highly charged and/or more weakly bound

clusters can be increased and the list of complete $^{DT}CCS_{He}$ values of observable clusters can be found in Table A.1 (see Appendix A).

From a visual inspection, it becomes apparent that protonated Phe forms various clusters over a wide range of sizes and charges. Amongst the identified clusters, the strongest peak occurs at $m/z = 331$ (Figure 4.1, top), which corresponds to the dimer with charge state +1 ($n/z = 2/1$). At different instrumental settings, clusters up to the 45-mer with the charge state +6 are observed for Phe (see Table A.1 in Appendix A). For singly charged species, no clusters containing more than two Phe molecules are observed. Doubly charged clusters start to appear from $n = 8$ and triply charged clusters from $n = 17$. This is in good agreement with the literature, where it was shown that AA cluster formation is accompanied by an increase in overall charge, since larger clusters can accommodate more charges.^{15, 68-69} Additionally, like most of the AAs, the intensity patterns within the mass spectra usually follow a smooth evolution with increasing n upon electrospray ionization.¹⁴⁻¹⁵ However, the dimer exhibits the highest abundance among all other clusters, and the dimer as an onset of aggregation raises the question if there is a special property within this dimer structure which then influences further cluster formation.

4.1.2 Side-Chain Monofluorination

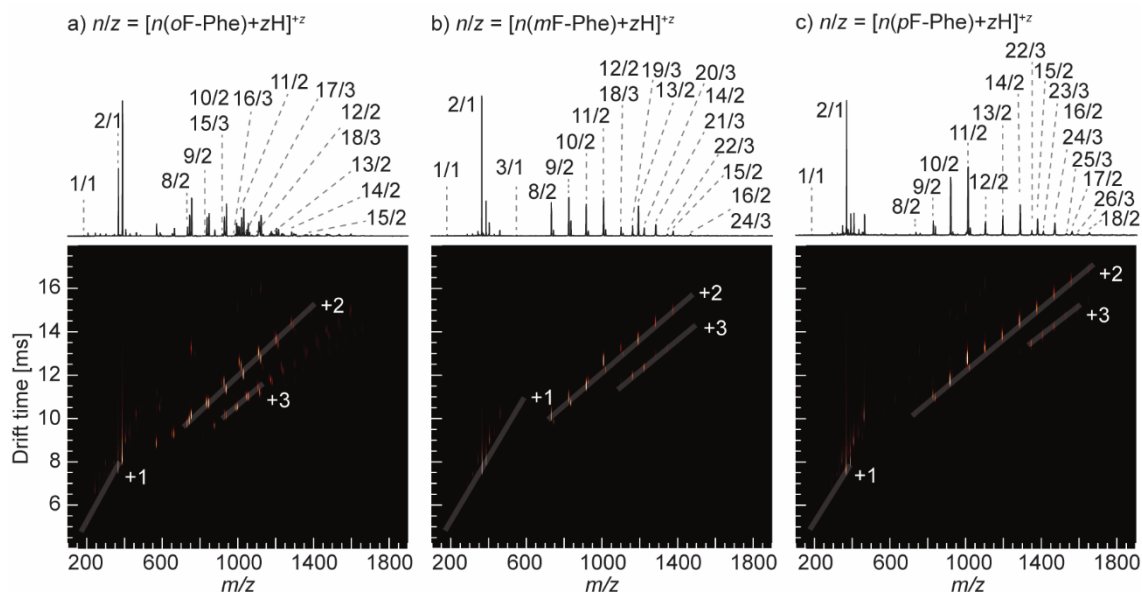


Figure 4.2 TOF mass spectra of protonated *ortho*-, *meta*- and *para*-fluorinated phenylalanine (top of a) *o*F-Phe, (b) *m*F-Phe and (c) *p*F-Phe and the corresponding drift time versus m/z plot (bottom). Individual clusters are labelled with n/z where n corresponds the number of respective monomers in the cluster and z the charge state. The singly, doubly and triply protonated clusters follow distinct growth trends and are marked with white lines in the drift time scans.

The influence of side-chain monofluorination of Phe has been mainly studied regarding protein stability and previous studies show that the subtle change in the position of fluorination can influence the enzymatic structure and function rigorously.^{27, 70-71} Previous studies have, however mostly focused on the influence of side-chain perfluorination on the aggregation propensity of Phe and little interest has been given to monofluorination of the side-chain.⁹⁻¹⁰ Here, IM-MS is utilized to investigate the cluster formation propensity of side-chain monofluorinated Phe derivatives. In following Chapters, the influence of subtle change in the position of the fluorine atom on the structure and interaction within Phe clusters will be examined. Figure 4.4 shows the mass spectrum (top) and two-dimensional drift time scans (bottom) of protonated, side-chain monofluorinated Phe derivatives (Figure 4.2 (a) *ortho*-, (b) *meta*- and (c) *para*-fluorophenylalanine) upon *n*-ESI of 5 mM enantiopure, aqueous solution. To obtain the spectra, same instrumental settings have been used as in the previous chapter (Figure 4.1) to enable direct comparison regarding the self-assembly propensity of the investigated systems. As shown in Figure 4.2, all three monofluorinated Phe isomers form a wide distribution of clusters up to charge state +3. At different instrumental settings, clusters up to $n/z = 26/4$ are observed for *o*F-Phe, up to $n/z = 24/3$ for *m*F-Phe, and up to $n/z = 36/4$ for *p*F-Phe. The list of complete,

experimentally obtained $^{DT}CCS_{He}$ values of observable monofluorinated Phe clusters are listed in Table B.1 (see Appendix B).

Generally, the overall peak patterns in the mass spectra (Figure 4.2, top) are similar to that of the non-fluorinated analogue (Phe, Figure 4.1), in which the dimer with charge state +1 ($n/z = 2/1$) is also the most abundant species as observed for all three monofluorinated Phe isomers. Within the three variations, para-monofluorination has the highest cluster formation propensity (see Table B.1 in Appendix B), whereas *ortho*-monofluorination of Phe seems to result in suppression of cluster formation. When taking a closer look at the spectrum of *o*F-Phe (Figure 4.2 (a)), sodium adducts are also visible ($M+23$ amu), beside the protonated species. By modulating the voltage of the ionization source, this problem could not be overcome, which is indicative of high salt content in the sample. This in turn may suppress and/or hinder cluster formation.

4.1.3 Side-Chain Perfluorination

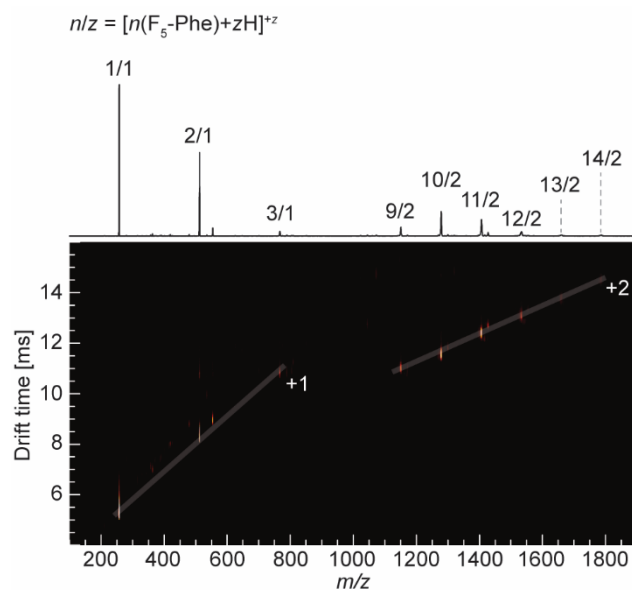


Figure 4.3 TOF mass spectrum of protonated pentafluorophenylalanine (top) and the corresponding two-dimensional drift time versus m/z plot (bottom). Individual clusters are labelled with n/z where n corresponds the number of Phe monomers in the cluster and z the charge state. The singly, doubly and triply protonated clusters follow distinct growth trends and are marked with white lines in the drift time scans.

Finally, the difference in self-assembly of Phe upon side-chain perfluorination is studied. Figure 4.3 shows the mass spectrum and the two-dimensional drift time scan of pentafluorophenylalanine ($\text{F}_5\text{-Phe}$) upon n ESI of 5 mM aqueous solution. In contrast to the monofluorinated Phe derivatives, $\text{F}_5\text{-Phe}$ only forms clusters up to charge state +2 ($z = 2$) at the same instrumental setting. Even at different instrumental settings, no additional clusters are observed. Only nine clusters are identified in total, which is by far less than the monofluorinated Phe derivatives, where 15–26 clusters were observed (see Table C.1 in Appendix C). Also, the singly charged monomer ($n/z = 1/1$) shows highest abundance, followed by the singly charged dimer ($n/z = 2/1$). This is in contrast to the protonated Phe (Figure 4.1) and monofluorinated Phe derivatives (Figure 4.4 (a)–(c)), where the $n/z = 2/1$ was always the most intense species in the mass spectra. This is very likely due to the instrumental setting – the monomers of Phe and its monofluorinated derivatives were below $m/z = 200$, where the transmission of the instrumental setting is quite low. For higher transmission of such small ions, a low m/z -setting is usually necessary.

4.2 Monomers

4.2.1 Phenylalanine

IM-MS coupled to gas-phase IR spectroscopy in the fingerprint region is an invaluable combination for probing the gas-phase structure of biomolecules^{38-40, 72-73} and mass-selective IR spectroscopy has also been extensively used to study AA in the gas phase.^{21, 53, 74} Therefore, to better understand the assembly propensity of Phe, the main building block – the singly protonated Phe monomer, $[\text{Phe}+\text{H}]^+$, is studied by drift-time and m/z -selective gas-phase IR spectroscopy (Figure 4.4).

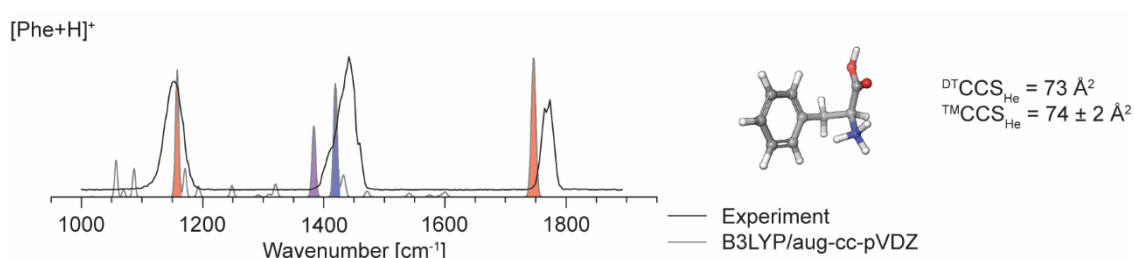


Figure 4.4 Size- and conformer-selected IRMPD spectrum of protonated phenylalanine monomer, $[\text{Phe}+\text{H}]^+$, (black trace) and theoretical vibrational spectrum obtained *via* calculations at the B3LYP/aug-cc-pVDZ level of theory (grey trace). Harmonic frequencies are scaled by a factor of 0.971.⁶⁴ The IR bands that correspond to neutral carboxylic acid vibrations are colored in red, the bands that stem from vibrations of protonated amine in blue, and the bands that arise due to the coupling of both modes in purple. On the right side, the corresponding low-energy geometry along with the experimental CCS ($^{\text{DT}}\text{CCS}_{\text{He}}$) and theoretically obtained CCS ($^{\text{TM}}\text{CCS}_{\text{He}}$) values are presented.

The black trace in Figure 4.4 represents the experimentally obtained IRMPD spectrum of $[\text{Phe}+\text{H}]^+$. Generally, three features are observed at 1750–1800 cm^{-1} , at 1400–1500 cm^{-1} and at 1100–1200 cm^{-1} . The experimental spectrum is compared to the calculated spectrum (Figure 4.4, grey trace) of the N-protonated, geometry-optimized, lowest-energy structure to assign the individual IR features. Here, the IR features related to vibrations of carboxylic acids are colored in red, amines in blue and the coupled mode of both vibrations in purple. The complete assignment of the IR bands can be found in Table A.2 (See Appendix A). In the experimental spectrum, the IR feature at 1770 cm^{-1} is assigned to the C=O stretch mode, $\nu(\text{C}=\text{O})$, and the feature at 1153 cm^{-1} to the neutral carboxylic acid bending mode, $\delta(\text{C}-\text{O}-\text{H})$. The IR band observed at 1141 cm^{-1} is assigned to the umbrella mode of protonated amine, $\delta_{\text{umb}}(\text{NH}_3^+)$. The low-wavenumber shoulder of this feature at 1415 cm^{-1} is attributed to the combination of the $\delta(\text{C}-\text{O}-\text{H})$ and $\delta_{\text{umb}}(\text{NH}_3^+)$ modes. The results are in good agreement with that observed in a

previous study, where the IRMPD spectrum of $[\text{Phe}+\text{H}]^+$ was obtained at an ion trap mass spectrometer coupled to the FEL, *via* electrospraying Phe from a solution of methanol/water (50/50 vol%) with 0.1% formic acid.⁷⁵ Within their work, the theoretical spectrum was calculated at the B3LYP/6-311++G(d,p) level and scaled by a factor of 0.9679 to incorporate anharmonicity and to fit their experimental spectrum.⁷⁶

The optimized geometry of $[\text{Phe}+\text{H}]^+$ is shown on the right side of Figure 4.4. A possible intramolecular interaction is the cation- π interaction between the charge carrier ($-\text{NH}_3^+$) and the aromatic side-chain. However, $-\text{NH}_3^+$ is not directed towards the exact center of the phenyl ring, rather to the edge. Thus, the geometry is not optimal in achieving cation- π interaction. It may be due to the constraint arising from the carbon backbone, as reported previously by Fu et al.⁷⁵ Rather, the $-\text{NH}_3^+$ group is positioned in a way that the hydrogen atom of the protonated amine is in close vicinity to the carboxylic acid ($-\text{C}=\text{O}$) group, thus forming an intramolecular interaction $\text{H}_2\text{N}^+-\text{H}\cdots\text{O}=\text{C}$. As a much stronger interaction than the cation- π interaction, this hydrogen bonding must be the key factor in the overall stability of the system. To further support the assignment, the experimentally obtained CCS value ($^{\text{DT}}\text{CCS}_{\text{He}} = 73 \text{ \AA}^2$) is compared to the theoretical calculation ($^{\text{TM}}\text{CCS}_{\text{He}} = 74 \pm 2 \text{ \AA}^2$), which is determined from the geometry-optimized, lowest-energy structure as presented on the right side of Figure 4.4. The $^{\text{TM}}\text{CCS}_{\text{He}}$ is in very good agreement with the experiment as is within the error of calculation.

4.2.2 Side-Chain Monofluorinated Phenylalanine Isomers

The side-chain monofluorinated Phe derivatives are further studied by size- and conformer-selective gas-phase IRMPD spectroscopy. First, the respective protonated monomers ($[(oF\text{-Phe})+H]^+$, $[(mF\text{-Phe})+H]^+$ and $[(pF\text{-Phe})+H]^+$) are studied in comparison to the non-fluorinated analogue ($[\text{Phe}+H]^+$). The black traces (Figure 4.5, left) represent the experimentally obtained spectra. In general, the common IR features are the bands at $\sim 1770\text{ cm}^{-1}$, the strong absorptions between $1400\text{--}1500\text{ cm}^{-1}$ and the strong feature at $1100\text{--}1200\text{ cm}^{-1}$. The shoulder of the most intense feature at $1400\text{--}1500\text{ cm}^{-1}$ appears at 1470 cm^{-1} in $[(oF\text{-Phe})+H]^+$ which is not as intense in the other isomers, and another feature appears at 1579 cm^{-1} for $[(pF\text{-Phe})+H]^+$. The newly arising feature when compared to that of $[\text{Phe}+H]^+$ is the weak feature at 1215 cm^{-1} for $[(oF\text{-Phe})+H]^+$, which is observed at higher wavenumber (approx. 1260 cm^{-1}), with increasing intensities for $[(mF\text{-Phe})+H]^+$ and $[(pF\text{-Phe})+H]^+$.

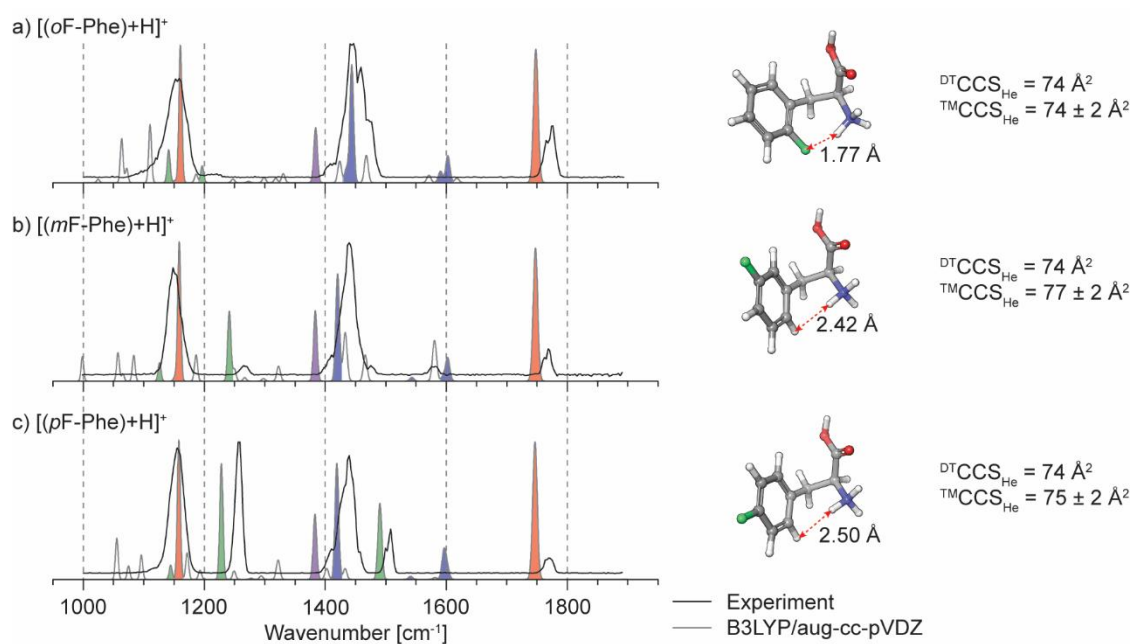


Figure 4.5 Size- and conformer-selected IRMPD spectra of protonated, (a) *ortho*-, (b) *meta*- and (c) *para*-fluorophenylalanine monomers (black trace) and theoretical vibrational spectrum obtained *via* calculations at the B3LYP/aug-cc-pVDZ level of theory (grey trace). Harmonic frequencies are scaled by a factor of 0.971.⁶⁴ The IR bands that correspond to neutral carboxylic acid vibrations are colored in red, protonated amine in blue, and the coupling of both modes in purple. IR features that arise due to vibrations of the C–F bonds are colored in green. The corresponding optimized geometries along with the experimental CCS ($^{DT}CCS_{He}$) and theoretically obtained CCS ($^{TM}CCS_{He}$) values are presented on the right side.

The experimental spectra are compared to the calculated spectra of the geometry-optimized, lowest-energy structures. The bands have been colored according to the respective modes of vibrations, as in Chapter 4.2.1. Additionally, colored in green are the IR bands associated with the C–F stretch modes, $\nu(\text{C–F})$. In all three experimental spectra, the common features at $\sim 1770\text{ cm}^{-1}$ and $\sim 1150\text{ cm}^{-1}$ correspond to $\nu(\text{C=O})$ and $\delta(\text{C–O–H})$ of a neutral carboxylic acid, respectively. The most intense, somewhat broader features at $1100\text{--}1200\text{ cm}^{-1}$ are assigned to $\delta_{\text{umb}}(\text{NH}_3^+)$, of which the shoulders at lower wavenumber are due to the coupled mode of $\delta_{\text{umb}}(\text{NH}_3^+)$ and $\delta(\text{C–O–H})$. These features are also observed and assigned similarly in the spectrum of $[\text{Phe+H}]^+$ (Chapter 4.2.1). The higher wavenumber shoulder of this most intense feature is assigned as the vibration of the phenyl ring. Interestingly, a strong, resolved feature is observed only in the spectrum of $[(p\text{F-Phe+H})]^+$ at 1490 cm^{-1} , which is assigned as the $\nu(\text{C–F})$ coupled to the vibration of the phenyl ring. The motion of the phenyl ring induces a stretching motion onto its substituent on the *para*-position, whereas the substituents on the *ortho*- and *meta*-position are forced to bending motions. Thus, for both $[(m\text{F-Phe+H})]^+$ and $[(p\text{F-Phe+H})]^+$, the $\nu(\text{C–F})$ mode is not observed.

The newly arising feature at $1150\text{--}1250\text{ cm}^{-1}$ in the monofluorinated isomer spectra when compared to the spectrum of $[\text{Phe+H}]^+$, is assigned as the $\nu(\text{C–F})$ mode, coupled to the vibration of the monofluorinated phenyl ring. Interestingly, this mode is much weaker and more red-shifted, by approximately 45 cm^{-1} , in the experimental spectrum of $[(o\text{F-Phe+H})]^+$ in contrast to its two isomers. This phenomenon can be explained on the basis of their respective global minimum conformers, presented on the right side of Figure 4.5. For $[(o\text{F-Phe+H})]^+$, the fluorine substituent of the phenyl ring is in close proximity to the protonated amine. The calculated $\text{C–F}\cdots\text{H–N}_2\text{H}^+$ internuclear distance is 1.77 \AA (see Figure 4.6), which is shorter than the sum of the van der Waals (vdW) radii (2.67 \AA , as $r_{\text{vdW}}(\text{H}) = 1.20\text{ \AA}$ and $r_{\text{vdW}}(\text{F}) = 1.47\text{ \AA}$)³⁷. Although the $\text{C–F}\cdots\text{H}$ angle of 106° (Figure 2.6) is not optimal for hydrogen bonding (usually optimal at an angle of 180°)³⁶, the short internuclear distance is indicative of an attractive intramolecular interaction, presumably charge-dipole interaction.^{36, 75} This argument can be supported by the red-shifted $\nu(\text{C–F})$ mode in the spectrum of $[(o\text{F-Phe+H})]^+$, in comparison to the other two isomers – the position of the fluorine atom in $[(m\text{F-Phe+H})]^+$ and $[(p\text{F-Phe+H})]^+$ is not ideal to form attractive $\text{C–F}\cdots\text{H}$ interaction with the protonated amine. Therefore, the free $\nu(\text{C–F})$ mode occurs at a higher wavenumber with elevated intensity. The complete assignment of the IR bands of the IRMPD spectra of $[(o\text{F-Phe+H})]^+$, $[(m\text{F-Phe+H})]^+$ and $[(p\text{F-Phe+H})]^+$ are listed in Table B.2–B.4, respectively (see Appendix B).

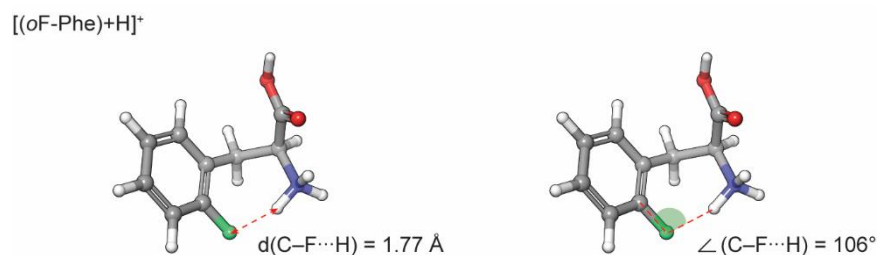


Figure 4.6 C–F⋯H internuclear distance, $d(\text{C}-\text{F}\cdots\text{H})$, and C–F⋯H bond angle, $\angle(\text{C}-\text{F}\cdots\text{H})$, of possible C–F⋯H interaction sites within the global minimum structure of [[*o*F-Phe)+H]⁺.

To add, the calculated $^{\text{TM}}\text{CCS}_{\text{He}}$ values of [[*o*F-Phe+H)]⁺ and [[*p*F-Phe+H)]⁺ are in good agreement with the experiment (0.0% and 1.4% deviation from the experiment, respectively) further supporting the assignment of the structure. Although the $^{\text{TM}}\text{CCS}_{\text{He}}$ value of [[*m*F-Phe+H)]⁺ is in good agreement with the experiment (3 Å² larger than the experiment with 4.0% deviation), it is conspicuous that the F atom on the phenyl ring is not in close proximity to the charge center, –NH₃⁺ (Figure 4.5 (c)), rather at the farther *meta*-position of the ring, relative to –NH₃⁺. To assure that no attractive interaction has been neglected in finding the global minimum structure, another low-energy structure (1.03 kJ mol⁻¹ above the global minimum), where the F atom is in closer proximity to the charge center, is compared to the global minimum structure (Figure 4.7). The two theoretical spectra are almost identical to each other regarding the IR band positions and relative intensities. No shift of the $\nu(\text{C}-\text{F})$ mode is observed, which indicates that the F atom on the *meta*-position of the aromatic ring is still too far from the charge center to engage in attractive C–F⋯H interactions. The two low-energy structures are also very similar, except for the position of the F atom on the phenyl ring, and are represented by the identical $^{\text{TM}}\text{CCS}_{\text{He}}$ values (77 Å²).

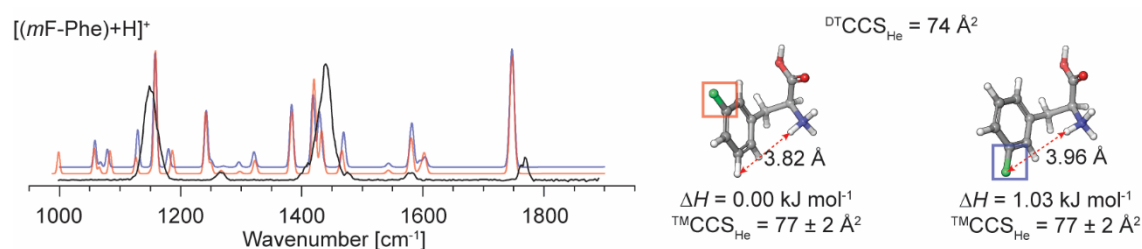


Figure 4.7 Size- and conformer-selected IRMPD spectrum of [[*m*F-Phe)+H]⁺ (black trace). The two low-energy spectra are presented in red and blue, where the site of fluorination of the phenyl ring are also marked with the corresponding color in the geometry-optimized, low-energy structures. The corresponding enthalpies relative to the global minimum structure at 298 K (ΔH) are presented below each structure together with the experimental ($^{\text{DT}}\text{CCS}_{\text{He}}$) and theoretical ($^{\text{TM}}\text{CCS}_{\text{He}}$) CCS values.

Although it is still under debate if such C–F \cdots H interaction can be categorized under hydrogen bonding or if it is more reasonable to be described as charge-dipole (or even dipole-dipole) interaction,³⁵ the results show that it is possible to identify such weak interactions in simple systems such as AA monomers via IM-MS-coupled IRMPD spectroscopy. This method is even sensitive towards subtle changes within the structure. Even if the overall size of the isomers are identical to each other, the site of fluorination within the aromatic ring can be differentiated the by means of the relative positions of the characteristic IR bands. Differentiation of such systems by IM-MS only or conventional solution-phase methods is nearly impossible.

4.2.3 Pentafluorophenylalanine

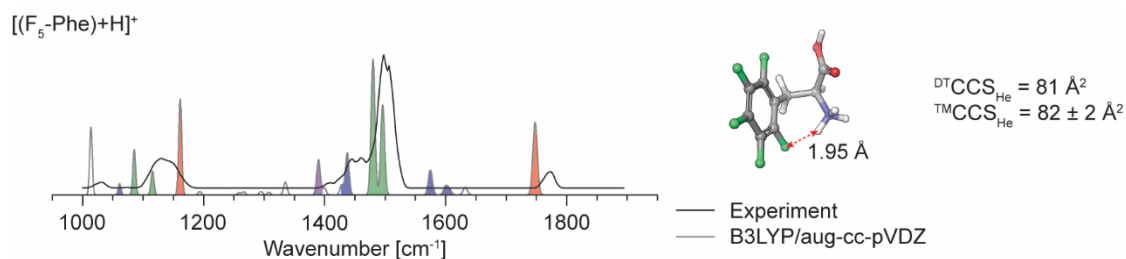


Figure 4.8 Size- and conformer-selected IRMPD spectrum of protonated pentafluorophenylalanine monomer (black trace) and theoretical vibrational spectrum obtained *via* calculations at the B3LYP/aug-cc-pVDZ level of theory (grey trace). Harmonic frequencies are scaled by a factor of 0.971.⁶⁴ The IR bands that correspond to neutral carboxylic acid vibrations are colored in red, protonated amine in blue, and combination of both modes in purple. IR features that arise due to vibrations of the C–F bonds are colored in green. The corresponding geometry-optimized low-energy structure along with the experimental CCS ($^{DT}CCS_{He}$) and theoretically obtained CCS ($^{TM}CCS_{He}$) values are presented on the right side.

In Figure 4.8, the IRMPD spectrum of protonated pentafluorophenylalanine monomer, $[(F_5\text{-Phe})+H]^+$ is presented with the black trace. The main observed features are the bands at 1750–1800 cm^{-1} , most intense feature at 1450–1550 cm^{-1} with a shoulder at 1400–1550 cm^{-1} and the band at 1100–1200 cm^{-1} . To assign the individual IR features, the experimental spectrum is compared to the theoretically calculated global minimum spectrum (Figure 4.8, grey trace). Colored in red are the modes associated with the neutral carboxylic acid vibrations, of which the band at 1772 cm^{-1} is assigned to $\nu(\text{C}=\text{O})$ and 1147 cm^{-1} to $\delta(\text{C}-\text{O}-\text{H})$. The most intense, partially resolved bands at 1496 and 1480 cm^{-1} arise due to the vibration of the pentafluorophenyl ($-\text{C}_5\text{F}_5$) ring and the shoulder at 1443–1462 cm^{-1} is assigned as the $\delta_{\text{umb}}(\text{NH}_3^+)$ mode coupled to the $\delta(\text{C}-\text{O}-\text{H})$ mode. The left part of the broad feature at 1124 cm^{-1} is assigned to the $\nu(\text{C}-\text{F})$ vibration of the $-\text{C}_5\text{F}_5$ ring. The complete assignment of the IR bands can be found in Table C.2 of Appendix C.

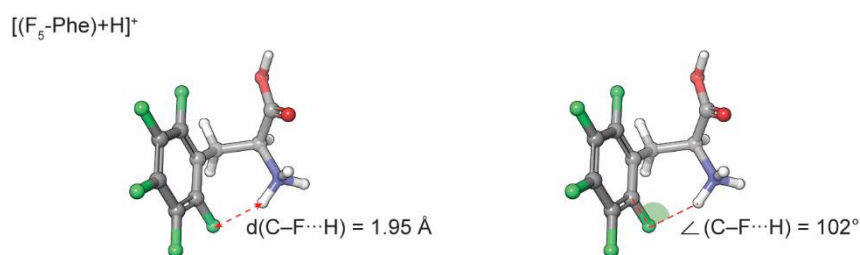


Figure 4.9 C–F \cdots H internuclear distance, $d(\text{C}-\text{F}\cdots\text{H})$, and C–F \cdots H bond angle, $\angle(\text{C}-\text{F}\cdots\text{H})$, of possible C–F \cdots H interaction sites within the global minimum structure of $[(\text{oF-Phe})+H]^+$.

Here, the calculated internuclear distance of C–F \cdots H–NH₂⁺ is quite close, with a value of 1.95 Å (Figure 4.9), similar to [(*o*F-Phe)+H]⁺. Although the angle between C–F \cdots H of 102° is not optimal for hydrogen bonding, the internuclear distance is shorter than the sum of the vdW radii of the two atoms and thus indicate an attractive charge-dipole (or dipole-dipole) interaction.³⁶⁻³⁷ The C–F \cdots H–NH₂⁺ internuclear distance is 0.18 Å longer than for [(*o*F-Phe)+H]⁺ whereas the overall structure seems similar regarding the position of the functional groups. It is probable that the F atom in [(*o*F-Phe)+H]⁺ is more negatively polarized than in [(F₅-Phe)+H]⁺, where the electron density of the phenyl ring has to be evenly distributed among five F atoms. Consequently, the C–F \cdots H is slightly weaker than in [(*o*F-Phe)+H]⁺, as indicated by the longer intranuclear distance. To add, the theoretically calculated CCS value (TMCCS_{He} = 82 ± 2 Å²) is in good agreement with the experimentally obtained ^{DT}CCS_{He} value of 81 Å².

4.3 Dimers

4.3.1 Phenylalanine

IM-MS-orthogonal gas-phase IR spectroscopy has also been used to study protonated AA dimers.^{21, 74} Figure 4.10 shows the drift time- and m/z -selected spectrum of the protonated Phe dimer, $[2\text{Phe}+\text{H}]^+$, obtained between 1000–1900 cm^{-1} . The IR features mainly originate from N–H bending modes and C=O and/or C–O stretching modes, as typically observed in AA dimers.^{8, 21-23, 53} The here-presented spectrum is in good agreement with that observed in a previous study, where it was shown that the dimer prefers a type A structure in which the side-chain geometry maximizes cation- π interaction between the aromatic side-chains and the positive charge on the $-\text{NH}_3^+\cdots\text{H}_2\text{N}-$ moiety.²¹ In comparison to its protonated monomer, $[\text{Phe}+\text{H}]^+$, the dimer can effectively form cation- π interaction, due to the larger conformational space and thus enabling non-covalent assembly between two building blocks. Therefore, the sandwich-like structure can be formed where the positive charge at the amine is stabilized between the two aromatic rings, as presented in Figure 4.10.

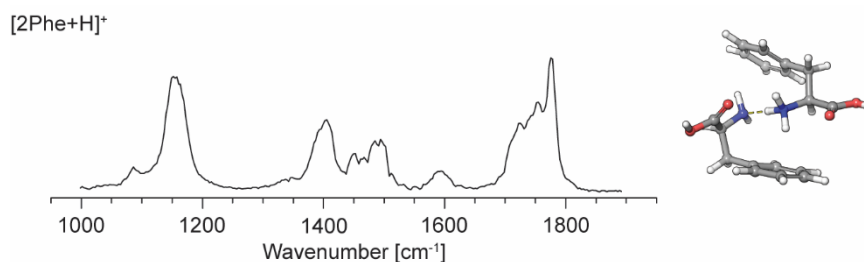


Figure 4.10. Size- and conformer-selected IRMPD spectrum of protonated phenylalanine dimer, $[2\text{Phe}+\text{H}]^+$. The optimized geometry of the lowest-energy structure is adapted from Seo et al.²¹

Previous studies show that for protonated AAs that do not have acidic or basic side-chains, the IR features not only help reveal the presence of hydrogen bonding within a structure but also help differentiate between charge-solvated and zwitterionic (Figure 2.3, type A, B and Z, respectively) structures. They can be easily differentiated from each other due to the absence of the $\nu(\text{O}-\text{C}-\text{O})$ mode, which is only present in AA dimers that contain a zwitterionic monomer. The two charge-solvated structures, on the other hand, can be readily distinguished based on intensity comparison of the two $\nu(\text{C}=\text{O})$ modes expected at 1600–1800 cm^{-1} . The one at higher wavenumber shows higher intensity in type A structures whereas it is the opposite for type B structures.²¹ These characteristic IR features will be used to determine the type of pairwise interaction and farther the structure of side-chain monofluorinated Phe dimer analogues.

4.3.2 Side-Chain Monofluorinated Phenylalanine Isomers

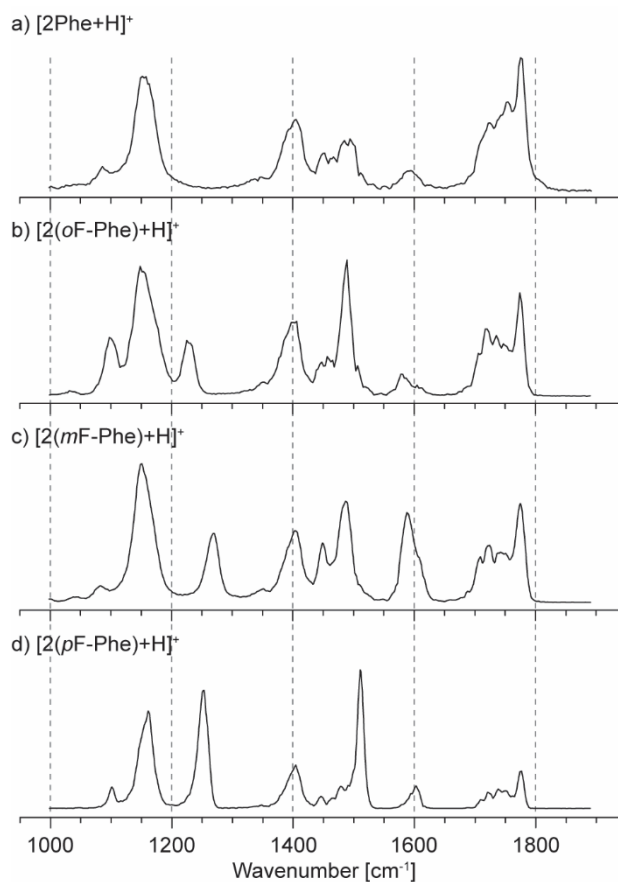


Figure 4.11 Size- and conformer-selected IRMPD spectra of protonated homodimer of (a) phenylalanine, (b) *ortho*-fluorophenylalanine, (c) *meta*-fluorophenylalanine and d) *para*-fluorophenylalanine.

Generally, the positions of the most intense IR bands of [2Phe+H]⁺ and its monofluorinated derivatives ([2(oF-Phe)+H]⁺, [2(mF-Phe)+H]⁺ and [2(pF-Phe)+H]⁺) are qualitatively similar (Figure 4.11 (a)–(d), respectively), which mainly originate from NH bending, C=O stretching and OH bending modes. The two bands at 1700–1800 cm⁻¹ indicate the presence of two non-zwitterionic carboxylic acid functional groups, both in different hydrogen bonding environments, as one feature is always red-shifted in the spectra. The relative intensities between the two features are not only similar within the spectra of the three fluorinated isomers (Figure 4.11 (b)–(d)), but also in that of their non-fluorinated analogue (Figure 4.11 (a)). One of the differences observable is the variable intensity of the band at 1600 cm⁻¹, which position usually corresponds to the bending mode of amines. Additionally, the feature at 1500 cm⁻¹ is more intense and resolved than in the spectrum of [2Phe+H]⁺, in the increasing order of [2(mF-Phe)+H]⁺ < [2(oF-Phe)+H]⁺ < [2(pF-Phe)+H]⁺. Lastly, from the two new features at 1100 and 1225–1275 cm⁻¹, the latter one is observed at slightly higher wavenumbers (~ 50 cm⁻¹)

for $[2(m\text{F-Phe})+\text{H}]^+$ and $[2(p\text{F-Phe})+\text{H}]^+$. To assign the underlying key interaction within the protonated, monofluorinated Phe homodimer derivatives, individual spectra are compared to the calculated spectra of the geometry-optimized, lowest-energy structures of types A, B and Z.

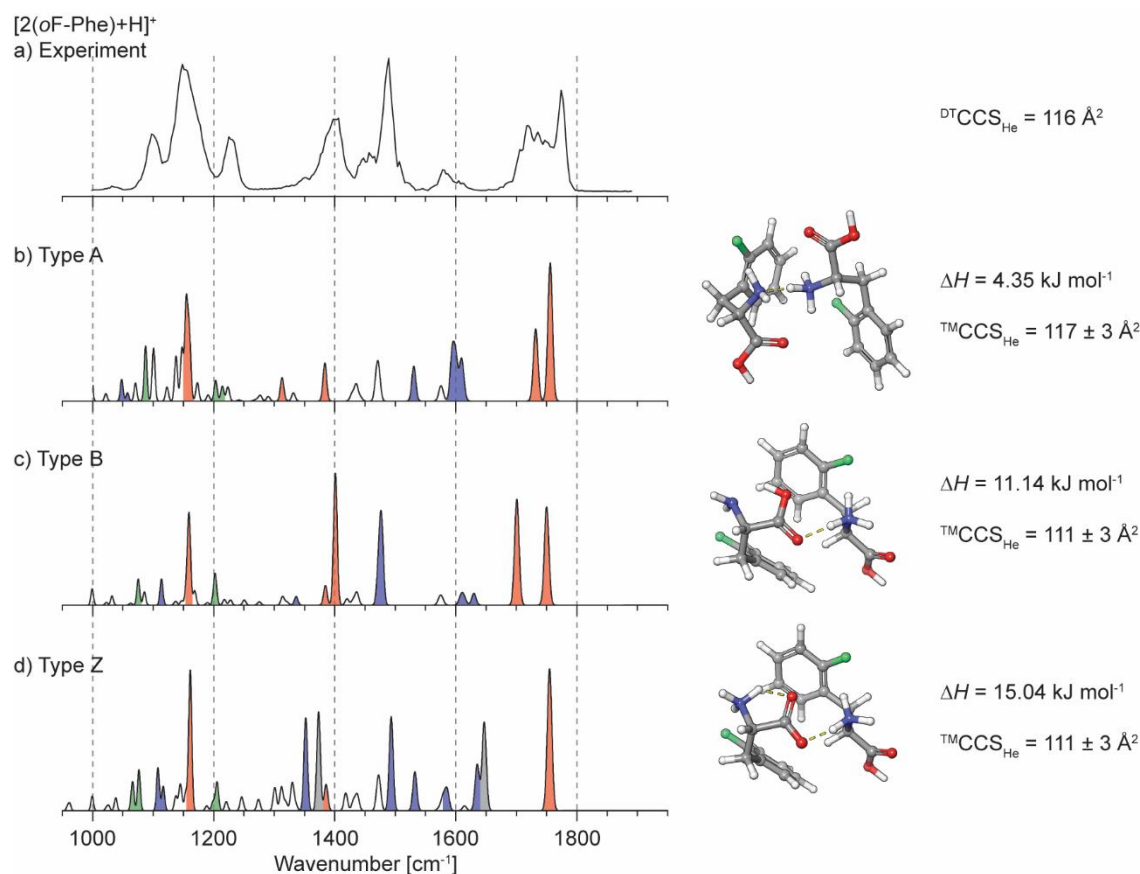
***Ortho*-fluorophenylalanine**

Figure 4.12 IRMPD spectra of (a) $[2(oF\text{-Phe})+H]^+$. Theoretical vibrational spectrum of $[2(oF\text{-Phe})+H]^+$ for types (b) A, (c) B and (d) Z structure are obtained via calculations at the B3LYP/aug-cc-pVDZ level of theory. Harmonic frequencies are scaled by a factor of 0.971.⁶⁴ The optimized geometries are represented at the right side of the corresponding theoretical spectra. IR bands that represent vibrations of neutral carboxyl groups ($-\text{COOH}$) are colored in red, deprotonated carboxylates ($-\text{COO}^-$) in grey and neutral or protonated amines ($-\text{NH}_2$ or $-\text{NH}_3^+$) in blue. IR features associated with vibrations of C-F bonds are colored in green. The corresponding optimized geometries along with the enthalpies relative to the global minimum structure at 298 K (ΔH), and the respective experimental CCS (${}^{\text{DT}}\text{CCS}_{\text{He}}$) and theoretically obtained CCS (${}^{\text{TM}}\text{CCS}_{\text{He}}$) values are presented on the right side.

The IRMPD spectrum of $[2(oF\text{-Phe})+H]^+$ is presented in Figure 4.12 (a), along with the theoretical spectra of low-energy structures of types A, B and Z (Figure 4.12 (b)–(d), respectively). The bands related to vibrations of neutral carboxylic acids ($-\text{COOH}$) are colored in red, carboxylates in grey ($-\text{COO}^-$), and neutral or protonated amines ($-\text{NH}_2$ or $-\text{NH}_3^+$) in blue. The IR bands that represent vibrations of C-F bonds are colored in green. In the experimental spectrum, the two features at 1773 and 1720 cm^{-1} are assigned to the $\nu(\text{C}=\text{O})$ stretching modes of two neutral carboxylic acids. This, along with the absence of strong bands

that correspond to the symmetric and antisymmetric $\nu(\text{O}-\text{C}-\text{O})$ modes of deprotonated carboxylate excludes the possibility of zwitterionic type Z structures. The relative intensities of the two $\nu(\text{C}=\text{O})$ modes at 1600–1800 cm^{-1} can be used to differentiate between type A and B structures. The $\nu(\text{C}=\text{O})$ mode at higher wavenumber exhibits higher intensity in the experimental spectrum and therefore agrees well with type A structure, whereas the opposite would be expected for type B structures. The small feature at 1617 cm^{-1} arises due to the $\delta_{\text{scis}}(\text{NH}_3^+)$ scissoring mode of protonated amine. The intense feature at 1487 cm^{-1} is assigned as the $\nu(\text{C}=\text{C})$ mode in combination with the $\delta(\text{C}-\text{H})$ mode of monofluorinated aromatic side-chains ($-\text{C}_6\text{H}_4\text{F}$). The feature at 1397 cm^{-1} is assigned to the C–OH stretch mode coupled to the C–O–H bending mode, $\nu(\text{C}-\text{OH}) + \delta(\text{C}-\text{O}-\text{H})$. The IR feature at 1228 cm^{-1} is assigned as the $\nu(\text{C}-\text{F})$ stretch mode of the $-\text{C}_6\text{H}_4\text{F}$ ring. Here, the two fluorine substituents at the *ortho*-position of each phenyl ring are in close proximity to the amines (2.35–2.63 Å, see Figure 4.13) and thus favor attractive intramolecular C–F \cdots H interactions. But the interaction angles are not equal to 180°, rather too small (77–108°, see Figure 4.13) and cannot be regarded as hydrogen bonding, rather as an electrostatic interaction. The intense band at 1154 cm^{-1} arises due to the $\nu(\text{C}-\text{OH}) + \delta(\text{C}-\text{O}-\text{H})$ mode, which is common in all three theory spectra (Figure 4.8 (b)–(d)) and are thus not serve to identify the type of interaction within the dimer. The feature at 1100 cm^{-1} is assigned as the combined $\delta_{\text{twist}}(\text{NH}_3^+)$ twist and the $\delta_{\text{wag}}(\text{CH}_2)$ wagging mode. The feature at 1097 cm^{-1} cannot be unambiguously assigned, as two features ($\delta_{\text{twist}}(\text{NH}_3^+)$ and $\nu(\text{C}-\text{F})$) are expected at similar values according to the theory, but only one is observed in the experiment.

[2(*o*F-Phe)+H]⁺

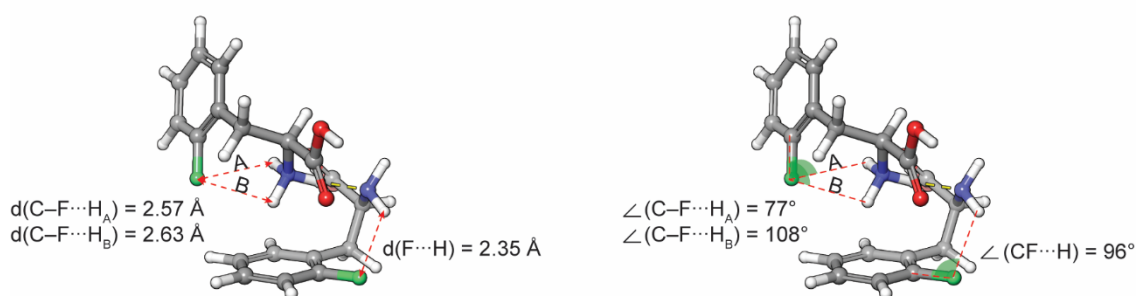


Figure 4.13 C–F \cdots H internuclear distances, $d(\text{C}-\text{F}\cdots\text{H})$, and C–F \cdots H bond angles, $\angle(\text{C}-\text{F}\cdots\text{H})$, of possible C–F \cdots H interaction sites within the low-energy structure of [2(*o*F-Phe)+H]⁺, with a type A interaction.

In overall, the low-energy spectrum of type A structure delivers the most similar features in the experimental spectrum of [2(*o*F-Phe)+H]⁺ but the spectrum of type B structure also

delivers similar band shapes and positions in the range of 1350–1600 cm^{-1} . In this structure, the protonated dimer is stabilized by the $-\text{NH}_3^+\cdots\text{H}_2\text{N}-$ hydrogen bonding where the positive charge on the amine is further stabilized by cation- π interaction with the aromatic side-chain of the other AA. The detailed assignment of the individual IR bands are listed in Table B.5 (Appendix B).

To further support the assignment, experimental $^{\text{DT}}\text{CCS}_{\text{He}}$ is compared to the theoretical calculations ($^{\text{TM}}\text{CCS}_{\text{He}}$) as presented on the right side of Figure 4.8. The $^{\text{TM}}\text{CCS}_{\text{He}}$ values are determined from the geometry-optimized, lowest-energy structures presented in Figure 4.12 (b)–(d), of which the enthalpy relative to the lowest energy structure at 298 K (ΔH) are also presented together with their respective structures. Although both types A and B low-energy structures deliver similar IR features, the experimental $^{\text{DT}}\text{CCS}_{\text{He}}$ value is in good agreement with type A structure (within 0.9%), whereas the $^{\text{TM}}\text{CCS}_{\text{He}}$ of type B structure deviates from the experiment by 4.3%. Not only can type Z structure be unambiguously excluded by IR band assignment, also is the calculated CCS value too small (5 \AA^2 smaller than the experimental value, with 4.3% deviation). The *ab initio* calculation also supports this assignment, as type A is energetically most stable among the three types of structures presented in Figure 4.12 (b)–(d).

However, the presented theoretical spectrum of type A in Figure 4.8 (b) is not the global minimum spectrum. Figure 4.14 presents the global minimum spectrum (Figure 4.14 (b)) and two other low-energy spectra (Figure 4.14 (c) and (d)) which are all obtained upon conformational search followed by DFT optimization with starting geometries of type A structures. The three spectra deliver similar IR features in the range of 1000–1650 cm^{-1} and the only observable difference between the spectra is the relative intensity of the two IR features at 1700–1800 cm^{-1} , where the third spectrum (type A III, 4.35 kJ mol^{-1} above the global minimum) delivers the best fit with the experimental spectrum. The two lower-energy spectra (Figure 4.14 (b) and (c)), however, show the opposite relative intensities of the two bands, which are usually typical for type B structures.

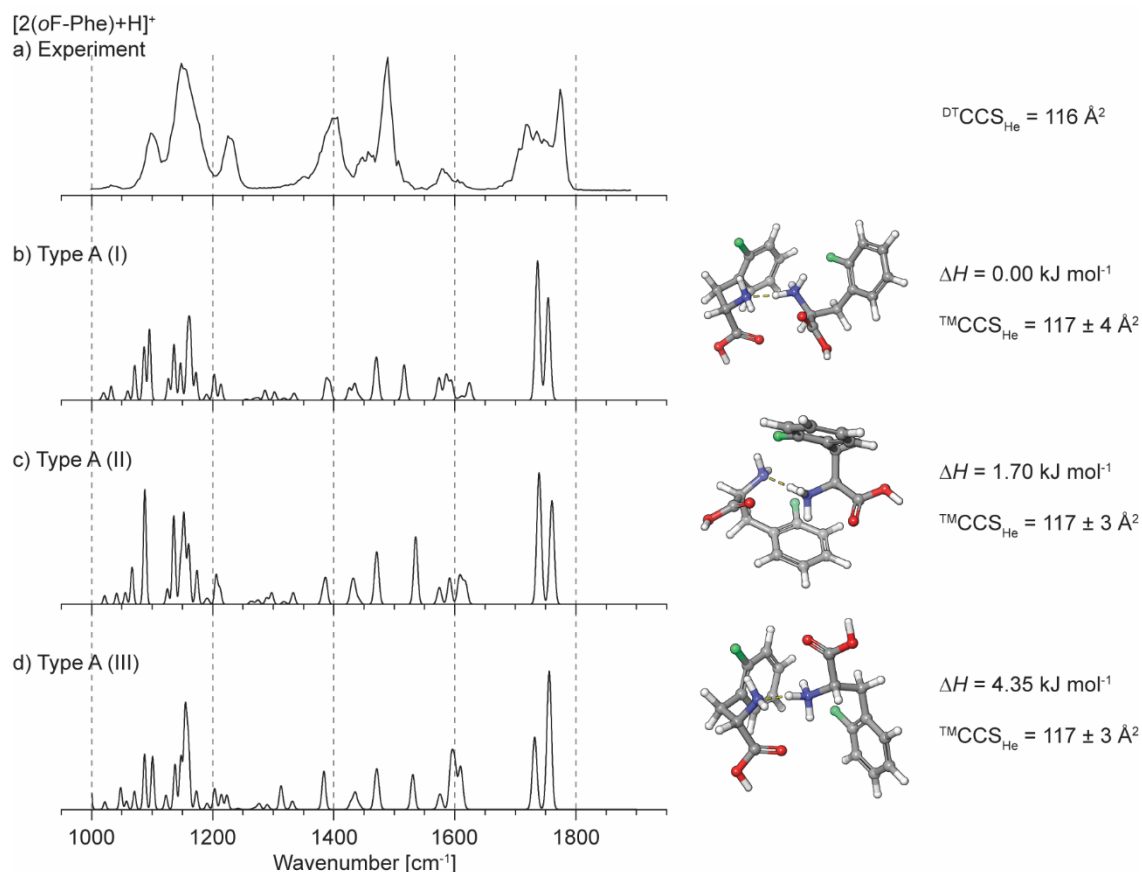


Figure 4.14 IRMPD spectrum of (a) $[2(oF\text{-Phe})+H]^+$ is compared to the theoretical spectra of type A low-energy structures ((b)–(d)). The corresponding optimized geometries along with the enthalpies relative to the global minimum structure at 298 K (ΔH), and the respective experimental CCS (${}^{\text{DT}}\text{CCS}_{\text{He}}$) and theoretically obtained CCS (${}^{\text{TM}}\text{CCS}_{\text{He}}$) values are presented on the right side.

Nonetheless, the calculated ${}^{\text{TM}}\text{CCS}_{\text{He}}$ values of all three structural candidates are in excellent agreement with the experiment, yet indistinguishable from each other due to the identical CCS values (117 \AA^2). The three structures differ in regards to the fine structure, but the protonated dimers are stabilized by $-\text{NH}_3^+ \cdots \text{H}_2\text{N}-$ hydrogen bonding in all three cases. The protonated amine points towards the center of the phenyl ring of the other AA favoring cation- π interaction. The small differences in their ${}^{\text{TM}}\text{CCS}_{\text{He}}$ values and their close-lying energies (ΔH) may be indicative of the presence of different structures within the probed ensemble.

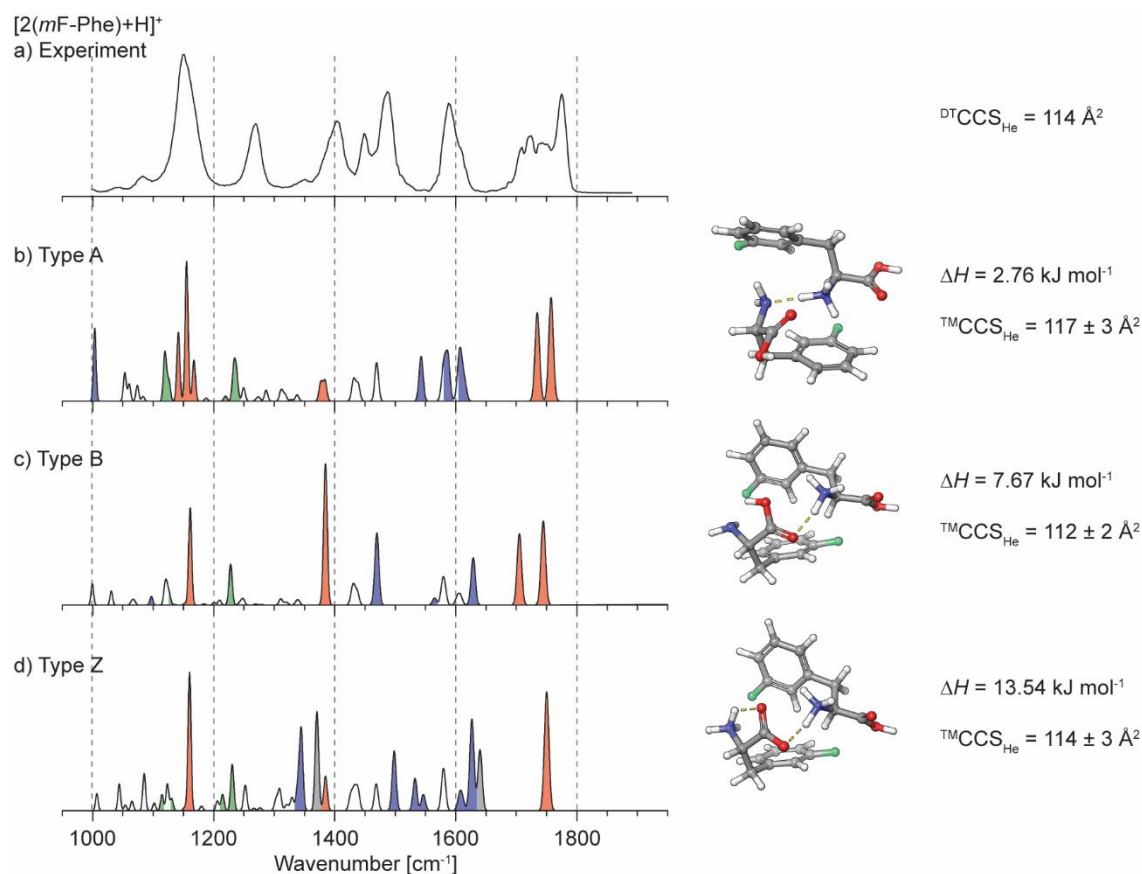
Meta-fluorophenylalanine

Figure 4.15 IRMPD spectrum of (a) $[2(mF\text{-Phe})+H]^+$. Theoretical vibrational spectrum of $[2(mF\text{-Phe})+H]^+$ for types (b) A, (c) B and (d) Z structure are obtained via calculations at the B3LYP/aug-cc-pVDZ level of theory. Harmonic frequencies are scaled by a factor of 0.971.⁶⁴ The optimized geometries are represented at the right side of the corresponding theoretical spectra. IR bands that represent vibrations of neutral carboxyl groups ($-\text{COOH}$) are colored in red, deprotonated carboxylates ($-\text{COO}^-$) in grey and neutral or protonated amines ($-\text{NH}_2$ or $-\text{NH}_3^+$) in blue. IR features that arise from vibrations of the C-F bonds are colored in green. The corresponding optimized geometries along with the enthalpies relative to the global minimum structure at 298 K (ΔH), and the respective experimental CCS ($^{\text{DT}}\text{CCS}_{\text{He}}$) and theoretically obtained CCS ($^{\text{TM}}\text{CCS}_{\text{He}}$) values are presented on the right side.

The experimentally obtained IRMPD spectrum of $[2(mF\text{-Phe})+H]^+$ (Figure 4.15 (a)) is presented with the theoretical spectra of low-energy structures of types A, B and Z (Figure 4.15 (b)–(d), respectively). The IR features in the experimental spectrum has been similarly assigned as described above for $[2(oF\text{-Phe})+H]^+$. The relative intensities of the two $\nu(\text{C}=\text{O})$ modes at 1600–1800 cm^{-1} together with the absence of strong symmetric and antisymmetric $\nu(\text{O}-\text{C}-\text{O})$

modes of deprotonated carboxylate indicate type A interaction. The feature at 1617 cm^{-1} is most intense in $[2(m\text{F-Phe})+\text{H}]^+$ among the three fluorinated isomers and is assigned as the $\delta_{\text{scis}}(\text{NH}_2)$ scissoring mode of the amine. Upon closer inspection of the structure, the hydrogen atoms of this amine are free from any attractive interactions. The phenyl rings point away, and the position of the neighboring carboxyl group is not optimal to achieve an intramolecular hydrogen bonding. The band at 1270 cm^{-1} arises due to the $\nu(\text{C-F})$ stretch vibration and is more blue-shifted than in the spectrum of $[2(m\text{F-Phe})+\text{H}]^+$ due to the absence of attractive $\text{C-F}\cdots\text{H}$ interaction. This bond is not weakened by any attractive, non-covalent interactions, thus occurs at a higher wavenumber. The assignment of the individual IR bands can be found in Table B.6 (Appendix B).

In general, the experimental spectrum of $[2(m\text{F-Phe})+\text{H}]^+$ is best represented by the theoretical spectrum of type A structure. The protonated dimer is stabilized by $-\text{NH}_3^+\cdots\text{H}_2\text{N}-$ hydrogen bonding, stabilized by attractive π -interaction from the aromatic side-chain. Furthermore, the theoretical $^{\text{TM}}\text{CCS}_{\text{He}}$ value of type A structure is in good agreement with the experimental $^{\text{DT}}\text{CCS}_{\text{He}}$ value with 2.6% deviation. *Ab initio* also supports this assignment, since types B and Z structures are 7.67 and 13.54 kJ mol^{-1} above the global minimum and also can be excluded by IR spectroscopy, although their theoretical $^{\text{TM}}\text{CCS}_{\text{He}}$ values are also in good agreement with the experiment (1.8% and 0.0% deviation, respectively).

Although the low-energy spectrum of type A structure is 2.76 kJ mol^{-1} above the global minimum, this spectrum is chosen as the best fit due to the above-mentioned reasons. To confirm the assignment, this theoretical spectrum is compared to the global minimum spectrum (Figure 4.16). The global minimum spectrum (type A I) and the low-energy spectrum (type A II, 2.76 kJ mol^{-1} above the global minimum) deliver similar features regarding the IR band shapes and positions. Overall, both theoretical spectra represent the experimental spectrum well and the calculated $^{\text{TM}}\text{CCS}_{\text{He}}$ values of their geometry-optimized structures are in good agreement with the experiment by 0.9 and 2.6%, respectively. But due to the opposite relative intensities of the two C=O bands at $1700\text{-}1800\text{ cm}^{-1}$, the global minimum spectrum is not considered as a good match. Nonetheless, due to the close-lying energies, it is believed that the two structures are coexistent within the probed ensemble.

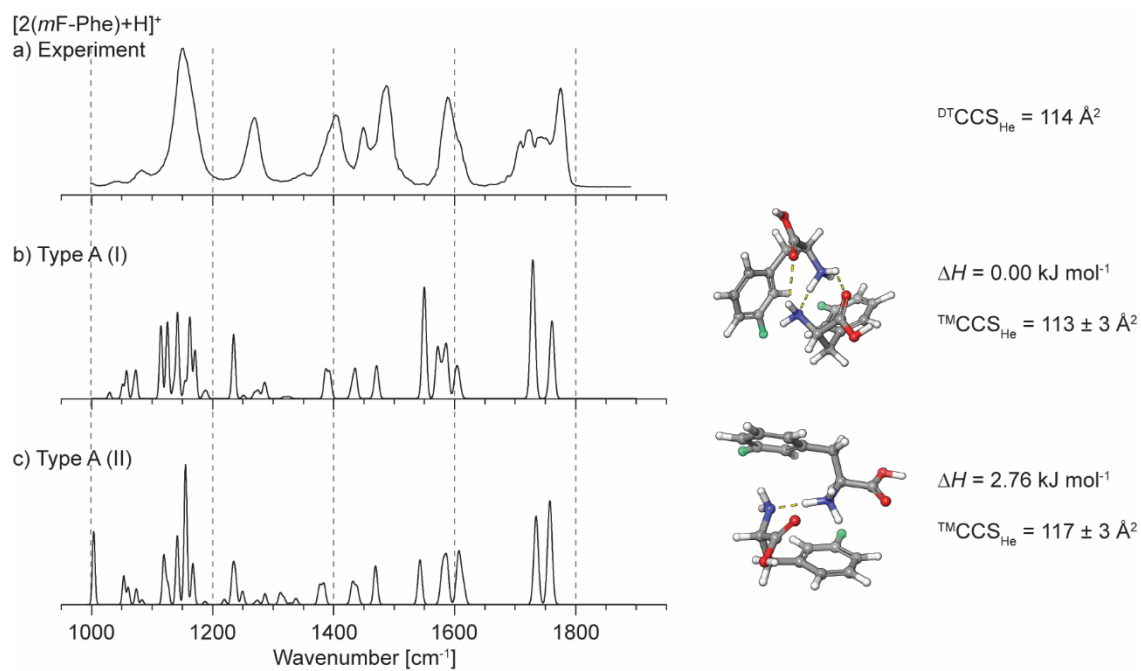


Figure 4.16 IRMPD spectrum of (a) [2(*m*F-Phe)+H]⁺ is compared to the theoretical spectra of type A low-energy structures ((b) and (c)). The corresponding optimized geometries along with the enthalpies relative to the global minimum structure at 298 K (Δ*H*), and the corresponding experimental CCS (^{DT}CCS_{He}) and theoretically obtained CCS (TMCCS_{He}) values are presented on the right side.

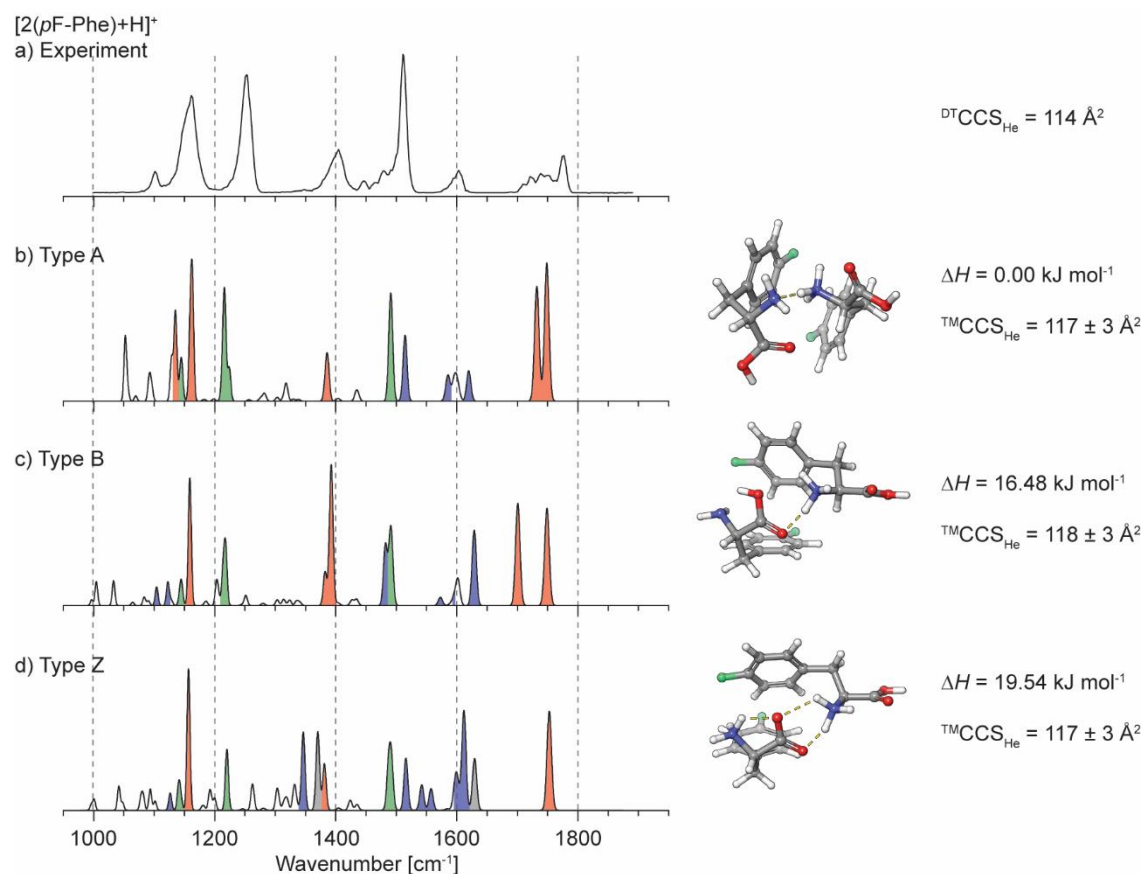
Para-fluorophenylalanine

Figure 4.17 IRMPD spectrum of (a) $[2(p\text{F-Phe})+\text{H}]^+$. Theoretical vibrational spectrum of $[2(p\text{F-Phe})+\text{H}]^+$ for types (b) A, (c) B and (d) Z structure are obtained via calculations at the B3LYP/aug-cc-pVDZ level of theory. Harmonic frequencies are scaled by a factor of 0.971.⁶⁴ The optimized geometries are represented at the right side of the corresponding theoretical spectra. IR bands that represent vibrations of neutral carboxyl groups ($-\text{COOH}$) are colored in red, deprotonated carboxylates ($-\text{COO}^-$) in grey and neutral or protonated amines ($-\text{NH}_2$ or $-\text{NH}_3^+$) in blue. IR features that arise due to vibrations of the C–F bonds are colored in green. The corresponding optimized geometries along with the enthalpies relative to the global minimum structure at 298 K (ΔH), and the respective experimental CCS ($^{\text{DT}}\text{CCS}_{\text{He}}$) and theoretically obtained CCS ($^{\text{TM}}\text{CCS}_{\text{He}}$) values are presented on the right side.

The experimental spectrum of $[2(p\text{F-Phe})+\text{H}]^+$ is compared to the theoretically determined spectra of types A, B and Z structures (Figure 4.17). The detailed assignment of the IR features are listed in Table B.7 of Appendix B. Since the detailed assignment of similar individual IR bands have been already done in the previous isomers, only significant differences will be discussed. The relative intensities of the two $\nu(\text{C}=\text{O})$ modes at 1600–1800 cm^{-1} together with

the absence of strong symmetric and antisymmetric $\nu(\text{O}-\text{C}-\text{O}^-)$ modes of deprotonated carboxylate indicate type A interaction. The most intense feature at 1511 cm^{-1} is assigned as the $\nu(\text{C}-\text{F})$ stretch vibration, in combination with the vibration of the aromatic ring ($-\text{C}_6\text{H}_4\text{F}$). This feature is most intense in $[2(p\text{F-Phe})+\text{H}]^+$ among the three fluorinated isomers (see Figure 4.11 (b)–(d)) and the intensity is associated with the largest change in the dipole moment upon the vibration of the C–F bond, at the *para*-position of the ring. Similarly, the other intense, well-resolved feature at 1253 cm^{-1} is again most intense in the spectrum of $[2(p\text{F-Phe})+\text{H}]^+$ also assigned to $\nu(\text{C}-\text{F})$. This mode is also more blue-shifted than in the spectrum of $[2(o\text{F-Phe})+\text{H}]^+$, since they are free from any attractive $\text{C}-\text{F}\cdots\text{H}$ interactions.

In general, the experimental spectrum of $[2(p\text{F-Phe})+\text{H}]^+$ is best represented by the theoretical spectrum of type A structure. The protonated dimer is stabilized by $-\text{NH}_3^+\cdots\text{H}_2\text{N}-$ hydrogen bonding, stabilized by an attractive π -interaction from the aromatic side-chain. Furthermore, the theoretical $^{\text{TM}}\text{CCS}_{\text{He}}$ value of type A structure is in excellent agreement (within the error of calculation, with 2.6% deviation from the experiment) with the experimental $^{\text{DT}}\text{CCS}_{\text{He}}$ value. Although types B and Z deliver similar $^{\text{TM}}\text{CCS}_{\text{He}}$ values (3.5% and 2.6% deviation from the experiment, respectively), *ab initio* calculation also supports the assignment, as type A structure is the global minimum structure and 16.48 and 19.54 kJ mol^{-1} higher in energy. This difference is more pronounced than in the previous cases (*ortho*- and *meta*-isomers).

4.3.3 Pentafluorophenylalanine

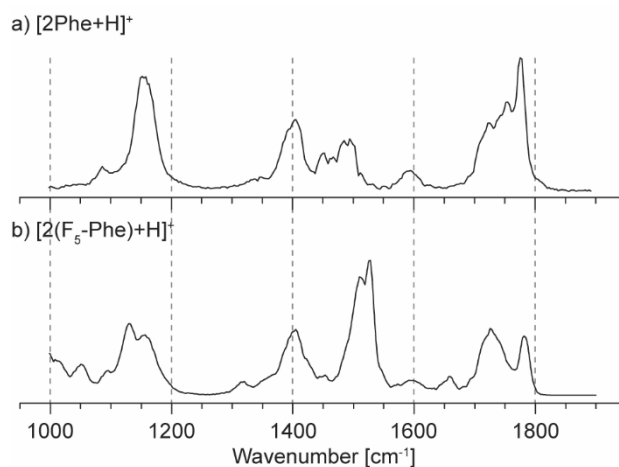


Figure 4.18 Size- and conformer-selected IRMPD spectra of protonated homodimer of (a) phenylalanine, $[2(\text{F-Phe})+\text{H}]^+$, and (b) pentafluorophenylalanine, $[2(\text{F}_5\text{-Phe})+\text{H}]^+$.

First, the IRMPD spectra of $[2\text{Phe}+\text{H}]^+$ and $[2(\text{F}_5\text{-Phe})+\text{H}]^+$ are compared with each other (Figure 4.18 (a) and (b), respectively). Generally, the positions of the most intense IR bands are qualitatively similar. The main differences observable are the changes in relative intensities of the two IR bands at $1700\text{--}1800\text{ cm}^{-1}$ and the appearance of a strong feature at $1460\text{--}1560\text{ cm}^{-1}$ in the spectrum of $[2(\text{F}_5\text{-Phe})+\text{H}]^+$.

To determine the intrinsic features within $[2(\text{F}_5\text{-Phe})+\text{H}]^+$, the experimental spectrum (Figure 4.19 a) is compared to the calculated spectra of the geometry-optimized, lowest-energy structures of types A, B and Z (Figure 4.19 (b)–(d), respectively). In the experimental spectrum, two features at 1726 and 1781 cm^{-1} are assigned to the $\nu(\text{C}=\text{O})$ stretching modes of two neutral carboxylic acids. This, along with the absence of strong bands that correspond to the symmetric and antisymmetric $\nu(\text{O}-\text{C}-\text{O})$ modes of deprotonated carboxylate rules out the presence of zwitterionic type Z structures. As mentioned in previous chapters, the relative intensities of the two $\nu(\text{C}=\text{O})$ modes at $1600\text{--}1800\text{ cm}^{-1}$ can be used to differentiate between type A and B structures. The $\nu(\text{C}=\text{O})$ mode at lower wavenumber exhibits higher intensity in the experimental spectrum and therefore agrees well with type B structure, whereas the opposite would be expected for type A structures.

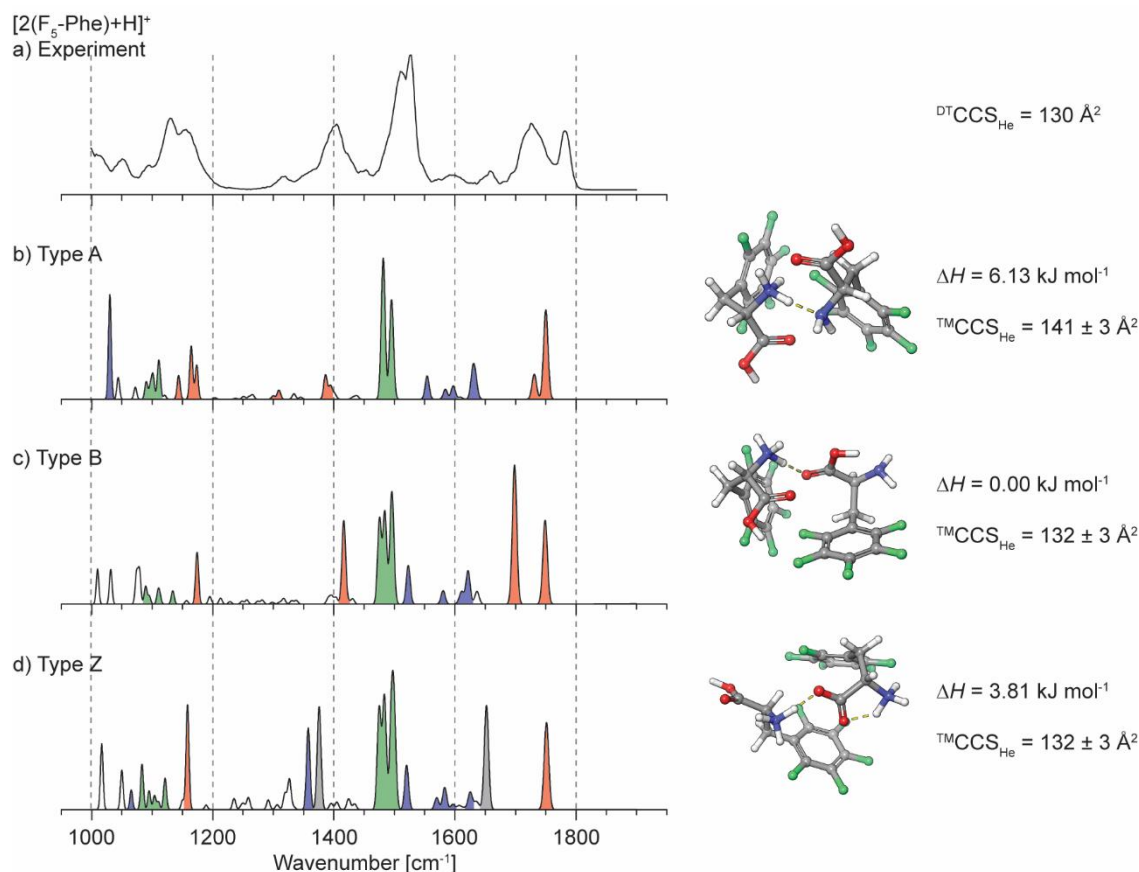


Figure 4.19 IRMPD spectrum of (a) $[2(\text{F}_5\text{-Phe})+\text{H}]^+$. Theoretical vibrational spectrum of $[2(\text{F}_5\text{-Phe})+\text{H}]^+$ for types (b) A, (c) B and (d) Z structure are obtained *via* calculations at the B3LYP/aug-cc-pVDZ level of theory. Harmonic frequencies are scaled by a factor of 0.971.⁶⁴ The optimized geometries are represented at the right side of the corresponding theoretical spectra. IR bands that represent vibrations of neutral carboxyl groups ($-\text{COOH}$) are colored in red, deprotonated carboxylates ($\text{O}-\text{C}-\text{O}$) in grey and neutral or protonated amines ($-\text{NH}_2$ or $-\text{NH}_3^+$) in blue. IR features that arise due to vibrations of the C-F bonds are colored in green. The corresponding optimized geometries along with the enthalpies relative to the global minimum structure at 298 K (ΔH), and the respective experimental CCS ($^{\text{DT}}\text{CCS}_{\text{He}}$) and theoretically obtained CCS ($^{\text{TM}}\text{CCS}_{\text{He}}$) values are presented on the right side.

The two most intense, partially resolved bands between $1460\text{--}1560 \text{ cm}^{-1}$ are assigned to the C=C stretching mode, $\nu(\text{C}=\text{C})$, combined with the C-F stretching, $\nu(\text{C}-\text{F})$, and the C-F bending mode, $\delta(\text{C}-\text{F})$, of the perfluorinated aromatic side-chains. The higher wavenumber peak of this band is associated with the $\nu(\text{C}-\text{F})$ mode of fluorine substituent on the *para*-position. The other fluorine atoms on *ortho*- and *meta*-position engage in a $\delta(\text{C}-\text{F})$ mode. The lower wavenumber peak is coupled to the $\delta(\text{C}-\text{F})$ mode of all fluorine atoms. Yet this feature is common in all three types of structures and does not serve to identify the type of interaction in

the dimer. Another intense feature at 1405 cm^{-1} is assigned to the combination of C–OH stretching and C–O–H bending modes, $\nu(\text{C–OH}) + \delta(\text{C–O–H})$. This is particularly intense for type B structure where the strong $\delta(\text{C–O–H})$ mode originates from a neutral carboxylic acid which is involved in an intramolecular $-\text{COOH}\cdots\text{NH}_2-$ interaction. Although the symmetric $\nu(\text{O–C–O})$ mode can also be present in this region, a deprotonated carboxylate is not considered a match here, due to the absence of its asymmetric $\nu(\text{O–C–O})$ mode expected at $1600\text{--}1650\text{ cm}^{-1}$. The two partially resolved bands at 1130 and 1157 cm^{-1} arise due to $\nu(\text{C–OH}) + \delta(\text{C–O–H})$ modes of a free carboxylic acid. Interestingly, type A structure delivers most similar features regarding the band shapes, whereas type B and Z structure only show one feature at $\sim 1160\text{ cm}^{-1}$. The less pronounced shoulder at 1093 cm^{-1} is assigned as the $\nu(\text{C–F})$ mode, which is common in all three theoretical spectra. Unlike the $\nu(\text{C–F})$ mode observed at a higher wavenumber ($1460\text{--}1560\text{ cm}^{-1}$), all fluorine atoms are involved in $\nu(\text{C–F})$ mode. However, the *ortho*- and *meta*-fluorine substituents engage in symmetrical vibration, and should thus be IR-inactive.

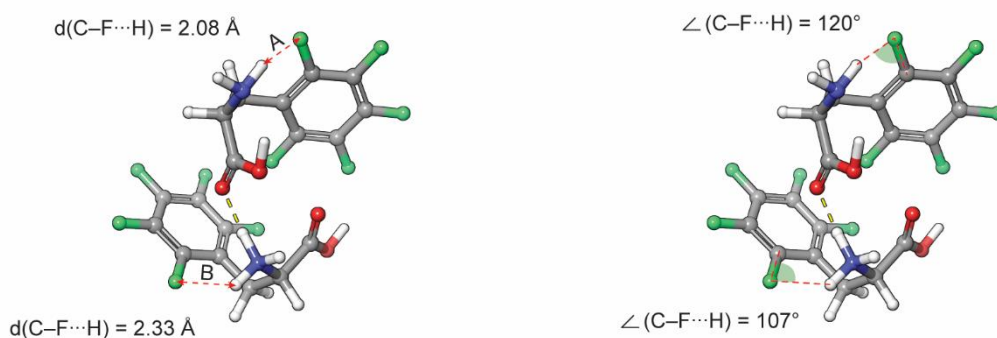


Figure 4.20 C–F \cdots H internuclear distances, $d(\text{C–F}\cdots\text{H})$, and C–F \cdots H bond angles, $\angle(\text{C–F}\cdots\text{H})$, of possible C–F \cdots H interaction sites within the low-energy structure of $[2(\text{F}_5\text{-Phe})+\text{H}]^+$, with a type B interaction.

In general, the theoretical spectrum of type B structure delivers the most similar features in the experimental spectrum of $[2(\text{F}_5\text{-Phe})+\text{H}]^+$ and the detailed assignment of the IR bands is listed in Table C.3 (see Appendix C). In type B structure, the protonated dimer is stabilized through the $-\text{NH}_3^+\cdots\text{HOOC}-$ interaction where the hydrogen bonding network spans the complete backbone of the two $\text{F}_5\text{-Phe}$ monomers. Here, the side-chains point away and do not provide additional charge-stabilization to the protonated amine, mainly due to the electron-poor nature of the perfluorinated phenyl ring. However, the fluorine substituents of on the *ortho*-position of the ring engage in attractive intramolecular C–F \cdots H interactions with amines in both AAs with an internuclear distance of 2.08 and 2.33 Å, and interaction angles of 107 and 120°,

respectively (Figure 4.20). These interactions are again not optimal to be classified as hydrogen bonding, rather as charge-dipole or dipole-dipole interactions.

In order to further support the assignment, experimental CCS value ($^{DT}CCS_{He}$) of $[2(F_5\text{-Phe})+H]^+$ was obtained and compared to theoretical calculations ($^{TM}CCS_{He}$) as presented on the right side of Figure 4.19. The $^{TM}CCS_{He}$ values are determined from the geometry-optimized, lowest-energy structures presented in Figure 4.19 (b)–(d), of which the enthalpies relative to the lowest energy structures at 298 K (ΔH) are also presented on the right side of Figure 4.19. The experimental $^{DT}CCS_{He}$ value is in good agreement with type B structure (within 1.5%), whereas the $^{TM}CCS_{He}$ of type A structure does not match well, deviating from the experiment by 11 Å² (8.5%). Although the $^{TM}CCS_{He}$ of type Z structure is in good agreement with $^{DT}CCS_{He}$ (1.5% deviation), its theoretical spectrum does not match the experiment. *Ab initio* calculation also supports this assignment, as type B is energetically most stable. However, the energy window predicted by theory is rather small since the ΔH of type A and type Z structures are only 6.13 and 3.81 kJ mol⁻¹ higher in energy. The differences in ΔH are not as pronounced as in the case of $[2\text{Phe}+H]^+$, where the structural candidates of other interaction types were separated by 23.5 kJ mol⁻¹ from the lowest-energy geometry.²¹ Whereas a type Z structure can be unambiguously excluded by IR spectroscopy, and the theoretical $^{TM}CCS_{He}$ of type A structure deviates from the experiment by 8.7%, the close-lying energetics may be indicative of the presence of coexisting structures within the probed ensemble of $[2(F_5\text{-Phe})+H]^+$. This may explain why some vibrational features from our experiment match well with those predicted for both type A as well as type B structures.

5 Conclusion and Outlook

Within this thesis, the structures of protonated monomer and homodimer of phenylalanine and its fluorinated derivatives – *ortho*-, *meta*-, *para*-fluorophenylalanine, and pentafluorophenylalanine have been determined using a combination of gas-phase IR spectroscopy in the 1000–1900 cm^{-1} fingerprint region combined with DFT calculations. Furthermore, the impact of mono- and perfluorination of the Phe side-chain on aggregation propensity was studied using IM-MS. Comparison of the experimental IR spectra and CCS values with the theoretical predictions show that it is possible to differentiate the monofluorinated Phe monomer derivatives by their distinct IR band positions whereby the differentiation is difficult by IM-MS only, due to the identical experimental CCS values. This method also enabled the identification of the interaction within the dimer system. In the case of monofluorinated Phe dimer derivatives, $[2(o\text{F-Phe})+\text{H}]^+$, $[2(m\text{F-Phe})+\text{H}]^+$ and $[2(p\text{F-Phe})+\text{H}]^+$ are stabilized by the hydrogen bond between a protonated amine of one AA and a neutral amine of the other AA. The $[2(\text{F}_5\text{-Phe})+\text{H}]^+$ is stabilized by the hydrogen bond between a protonated amine and a neutral carboxyl group of the other counterpart. This is in contrast to its non-fluorinated analogue, $[2\text{Phe}+\text{H}]^+$, where a protonated amine interacts with a neutral amine and the positive charge is stabilized by the interacting side-chain. The considerably different type of interaction in $[2\text{Phe}+\text{H}]^+$ and $[2(\text{F}_5\text{-Phe})+\text{H}]^+$ is largely caused by the reduced electron density of the perfluorinated aromatic ring. In contrast to $[2\text{Phe}+\text{H}]^+$ where the positive charge is stabilized by the aromatic system, no charge-stabilization is observed for $[2(\text{F}_5\text{-Phe})+\text{H}]^+$. Interestingly, this shift in electron density also has a tremendous impact on the aggregation propensity of both AAs. While Phe readily assembles into large clusters up to a 45mer, only smaller clusters were observed for $\text{F}_5\text{-Phe}$. This indicates that a change in the mode of interaction in dimers can have a significant impact on the tendency to self-assembly into larger clusters. The data indicate that there is a strong correlation between the pairwise interaction within the AA dimer, as the onset of aggregation, and the respective AA aggregation propensity. An in-depth understanding of the basic interactions on the AA dimer level is therefore crucial to predict the aggregation properties of larger systems, such as peptides or small proteins.

As an outlook, the IRMPD spectra of higher clusters of $\text{F}_5\text{-Phe}$ are presented in Figure 5.1. The relative positions and intensities of the IR features of the doubly protonated $\text{F}_5\text{-Phe}$ nonamer, $[9(\text{F}_5\text{-Phe})+2\text{H}]^{+2}$, and dodecamer, $[12(\text{F}_5\text{-Phe})+2\text{H}]^{+2}$, exhibit similar characteristics.

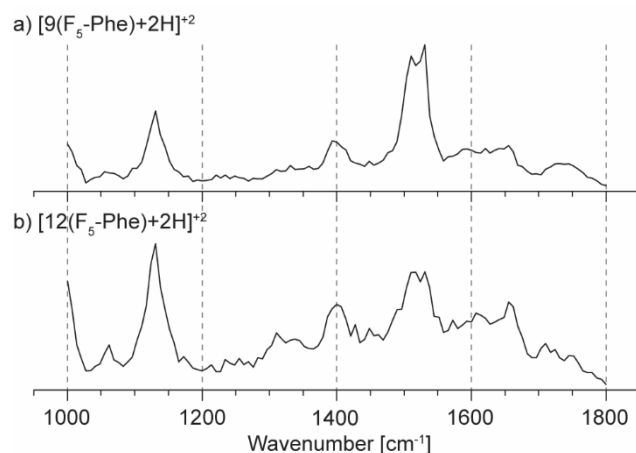


Figure 5.1 Size- and conformer-selected IRMPD spectra of doubly protonated clusters of pentafluorophenylalanine, where (a) $[9(\text{F}_5\text{-Phe})+2\text{H}]^{+2}$ and (b) $[12(\text{F}_5\text{-Phe})+2\text{H}]^{+2}$.

In the spectra of higher clusters, the IR bands exhibit characteristics of zwitterionic AAs. The higher charge within the clusters must be mainly stabilized *via* electrostatic interactions between the zwitterionic AAs, because the perfluorinated phenyl ring cannot stabilize the positive charge within the system. Also, the IR bands are broader, and the spectrum of the doubly protonated $\text{F}_5\text{-Phe}$ dodecamer is very congested, indicative of an increased conformational complexity within the system. To overcome this problem, the experiments could be conducted at cold temperatures, for e.g. utilizing superfluid helium nanodroplets (at 0.37 K), which delivers better resolution due to narrower IR bands and therefore allow easier interpretation of the spectra.⁷⁷ However, to better understand the intrinsic feature within the clusters, more refined theoretical calculations are necessary. Also, thorough conformational sampling is necessary to involve more random conformations that can be further optimized using DFT calculations. Nonetheless, the difficulty of theoretical computation of fluorinated molecules is that incorporation of fluorine not only withdraws electron density from its neighbors, but also induces change of electronic structures.⁷⁸ The use of different methods, such as the second-order Møller-Plesset (MP2) method,⁷⁹ could deliver more precise results, which accurately describes the electrostatic and dispersion components of hydrogen bonds.³⁶

Last but not least, the study of AAs with aliphatic side-chain are also subject for further investigations. The side-chain of aliphatic AAs are also known for their tendencies of accumulating and interacting at hydrophobic sites of proteins.⁴ By studying the influence of side-chain fluorination on the type of interaction and structure of monomers and dimers would deliver a better insight of their hydrophobic character, as well as potential $\text{C-F}\cdots\text{H}$ interactions, without the influence from e.g. aromatic systems.

6 References

1. Tenidis, K., et al., *J. Mol. Biol.* **2000**, 295 (4), 1055.
2. Arrasate, M.; Finkbeiner, S., *Exp. Neurol.* **2012**, 238 (1), 1.
3. Ghulam, M. A., et al., *CNS Neurol. Disord. Drug Targets* **2014**, 13 (7), 1280.
4. Salwiczek, M.; Nyakatura, E. K.; Gerling, U. I. M.; Ye, S.; Kokschi, B., *Chem. Soc. Rev.* **2012**, 41 (6), 2135.
5. Nomura, T., et al., *Biopolymers* **2011**, 95 (6), 410.
6. Woll, M. G.; Hadley, E. B.; Mecozzi, S.; Gellman, S. H., *J. Am. Chem. Soc.* **2006**, 128 (50), 15932.
7. West, A. P.; Mecozzi, S.; Dougherty, D. A., *J. Phys. Org. Chem.* **1997**, 10 (5), 347.
8. Fu, W., et al., *J. Mol. Spectrosc.* **2016**, 330, 194.
9. Senguen, F. T., et al., *Mol. Biosyst.* **2011**, 7 (2), 486.
10. Profit, A. A.; Vedad, J.; Saleh, M.; Desamero, R. Z. B., *Arch. Biochem. Biophys.* **2015**, 567, 46.
11. Schalley, C. A.; Weis, P., *Int. J. Mass Spectrom.* **2002**, 221 (1), 9.
12. Bush, M. F.; O'Brien, J. T.; Prell, J. S.; Saykally, R. J.; Williams, E. R., *J. Am. Chem. Soc.* **2007**, 129 (6), 1612.
13. Schmidt, J.; Kass, S. R., *J. Phys. Chem. A* **2013**, 117 (23), 4863.
14. Nemes, P.; Schlosser, G.; Vékey, K., *J. Mass Spectrom.* **2005**, 40 (1), 43.
15. Do, T. D., et al., *Anal. Chem.* **2016**, 88 (1), 868.
16. Cooks, R. G.; Zhang, D.; Koch, K. J.; Gozzo, F. C.; Eberlin, M. N., *Anal. Chem.* **2001**, 73 (15), 3646.
17. Kong, X., et al., *Angew. Chem. Int. Ed.* **2006**, 45 (25), 4130.
18. Rajabi, K.; Fridgen, T. D., *J. Phys. Chem. A* **2008**, 112 (1), 23.
19. Feng, R.-X.; Mu, L.; Yang, S.-M.; Kong, X.-L., *Chin. Chem. Lett.* **2016**, 27 (4), 593.
20. Feng, R.; Yin, H.; Kong, X., *Rapid Commun. Mass Spectrom.* **2016**, 30 (S1), 24.
21. Seo, J., et al., *Int. J. Mass Spectrom.* **2018**, 429, 115.

22. Linder, R.; Seefeld, K.; Vavra, A.; Kleinermanns, K., *Chem. Phys. Lett.* **2008**, *453* (1), 1.
23. Ieritano, C., et al., *PCCP* **2016**, *18* (6), 4704.
24. Alahmadi, Y. J.; Gholami, A.; Fridgen, T. D., *PCCP* **2014**, *16* (48), 26855.
25. Wu, R.; McMahon, T. B., *J. Am. Chem. Soc.* **2007**, *129* (16), 4864.
26. Cornilescu, G., et al., *Protein Sci.* **2007**, *16* (1), 14.
27. Budisa, N.; Wenger, W.; Wiltschi, B., *Mol. Biosyst.* **2010**, *6* (9), 1630.
28. Akiko, A.; Takeshi, Y.; Mitsunobu, D., *J. Pept. Sci.* **2014**, *20* (10), 794.
29. Adler-Abramovich, L., et al., *Nat. Chem. Biol.* **2012**, *8*, 701.
30. Mossou, E., et al., *Acta Crystallogr. A* **2014**, *70* (3), 326.
31. Do, T. D.; Kincannon, W. M.; Bowers, M. T., *J. Am. Chem. Soc.* **2015**, *137* (32), 10080.
32. Banik, D.; Kundu, S.; Banerjee, P.; Dutta, R.; Sarkar, N., *J. Phys. Chem. B* **2017**, *121* (7), 1533.
33. Martynyuk, A. E., et al., *Mol. Genet. Metab.* **2005**, *86*, 34.
34. Böhm, H.-J., et al., *ChemBioChem* **2004**, *5* (5), 637.
35. O'Hagan, D., *Chem. Soc. Rev.* **2008**, *37* (2), 308.
36. D'Oria, E.; Novoa, J. J., *CrystEngComm* **2008**, *10* (4), 423.
37. Bondi, A., *J. Phys. Chem.* **1964**, *68* (3), 441.
38. Seo, J., et al., *Angew. Chem. Int. Ed.* **2016**, *55* (45), 14173.
39. Seo, J.; Warnke, S.; Pagel, K.; Bowers, M. T.; von Helden, G., *Nat. Chem.* **2017**, *9*, 1263.
40. Hoffmann, W., et al., *J. Am. Chem. Soc.* **2018**, *140* (1), 244.
41. Khanal, N.; Masellis, C.; Kamrath, M. Z.; Clemmer, D. E.; Rizzo, T. R., *Analyst* **2018**, *143* (8), 1846.
42. Linder, R.; Nispel, M.; Häber, T.; Kleinermanns, K., *Chem. Phys. Lett.* **2005**, *409* (4), 260.
43. de Hoffmann, E.; Stroobant, V., *Mass Spectrometry: Principles and Applications, 3rd Edition*. Wiley-Interscience: 2007.
44. Uetrecht, C.; Rose, R. J.; van Duijn, E.; Lorenzen, K.; Heck, A. J. R., *Chemical Society Reviews* **2010**, *39* (5), 1633.
45. Nanita, S. C.; Cooks, R. G., *Angew. Chem. Int. Ed.* **2006**, *45* (4), 554.

46. Gogichaeva, N. V.; Williams, T.; Alterman, M. A., *J. Am. Soc. Mass. Spectrom.* **2007**, *18* (2), 279.
47. Yang, P.; Xu, R.; Nanita, S. C.; Cooks, R. G., *J. Am. Chem. Soc.* **2006**, *128* (51), 17074.
48. Spencer, E. A. C.; Ly, T.; Julian, R. R., *Int. J. Mass Spectrom.* **2008**, *270* (3), 166.
49. Fenn, J. B., *Angew. Chem.* **2003**, *115* (33), 3999.
50. Mason, E. A.; McDaniel, E. W., *Transport Properties of Ions in Gases*. Wiley-VCH: New York, 2005.
51. Oomens, J.; Sartakov, B. G.; Meijer, G.; von Helden, G., *Int. J. Mass Spectrom.* **2006**, *254* (1–2), 1.
52. Litvinov R , I; Faizullin D , A; Zuev Y , F; Weisel J , W., *Biophys. J.* **2012**, *103* (5), 1020.
53. Oomens, J.; Steill, J. D.; Redlich, B., *J. Am. Chem. Soc.* **2009**, *131* (12), 4310.
54. Schütz, M., et al., *Chem. Eur. J.* **2016**, *22* (24), 8124.
55. Hobza, P.; Havlas, Z., *Chem. Rev.* **2000**, *100* (11), 4253.
56. Socrates, G., *Infrared and Raman Characteristic Group Frequencies : Tables and Charts*. 3rd ed.; John Wiley & Sons, Ltd.: Chichester; New York, 2001.
57. Warnke, S.; Baldauf, C.; Bowers, M. T.; Pagel, K.; von Helden, G., *J. Am. Chem. Soc.* **2014**, *136* (29), 10308.
58. Warnke, S., et al., *J. Am. Chem. Soc.* **2015**, *137* (12), 4236.
59. Kliman, M.; May, J. C.; McLean, J. A., *Biochim. Biophys. Acta* **2011**, *1811* (11), 935.
60. *Schrödinger Release 2016-4: MacroModel*, Schrödinger, LLC: New York, NY, 2016.
61. Harder, E., et al., *J. Chem. Theory Comput.* **2016**, *12* (1), 281.
62. Frisch, M. J., et al. *Gaussian 16 Rev. A.03*, Wallingford, CT, 2016.
63. Grimme, S.; Antony, J.; Ehrlich, S.; Krieg, H., *J. Chem. Phys.* **2010**, *132* (15), 154104.
64. Merrick, J. P.; Moran, D.; Radom, L., *J. Phys. Chem. A* **2007**, *111* (45), 11683.
65. Millam, R. D. T. A. K. J. M. *GaussView*, Semichem Inc., Shawnee Mission, KS: 2016.
66. Mesleh, M. F.; Hunter, J. M.; Shvartsburg, A. A.; Schatz, G. C.; Jarrold, M. F., *J. Phys. Chem.* **1996**, *100* (40), 16082.
67. Shvartsburg, A. A.; Jarrold, M. F., *Chem. Phys. Lett.* **1996**, *261* (1), 86.

68. Myung, S.; Julian, R. R.; Nanita, S. C.; Cooks, R. G.; Clemmer, D. E., *J. Phys. Chem. B* **2004**, *108* (19), 6105.
69. Myung, S., et al., *J. Am. Chem. Soc.* **2006**, *128* (33), 10833.
70. Dominguez, M. A.; Thornton, K. C.; Melendez, M. G.; Dupureur, C. M., *Proteins: Struct., Funct., Bioinf.* **2001**, *45* (1), 55.
71. Mehta, K. R.; Yang, C. Y.; Montclare, J. K., *Mol. Biosyst.* **2011**, *7* (11), 3050.
72. Masellis, C.; Khanal, N.; Kamrath, M. Z.; Clemmer, D. E.; Rizzo, T. R., *J. Am. Soc. Mass. Spectrom.* **2017**, *28* (10), 2217.
73. Scutelnic, V., et al., *J. Am. Chem. Soc.* **2018**, *140* (24), 7554.
74. Ma, L.; Ren, J.; Feng, R.; Zhang, K.; Kong, X., *Chin. Chem. Lett.* **2018**.
75. Fu, W., et al., *Phys. Chem. Chem. Phys.* **2017**, *19* (1), 729.
76. Andersson, M. P.; Uvdal, P., *J. Phys. Chem. A* **2005**, *109* (12), 2937.
77. Mucha, E., et al., *Angew. Chem. Int. Ed.* **2017**, *56* (37), 11248.
78. Kaupp, M., *J. Comput. Chem.* **2007**, *28* (1), 320.
79. Møller, C.; Plesset, M. S., *Phys. Rev.* **1934**, *46* (7), 618.

Appendix A

Phenylalanine

Experimental collision cross-section ($^{DT}CCS_{He}$) values

Table A.1 Experimentally obtained $^{DT}CCS_{He}$ values of protonated Phe clusters where n corresponds to the number of amino acid monomer and z the charge state of the cluster.

$[n(\text{Phe})+z\text{H}]^{+z}$		
n	z	$^{DT}CCS_{He} [\text{\AA}^2]$
1	1	73
2	1	111
8	2	304
9	2	329
10	2	348
11	2	379
12	2	399
13	2	414
14	2	436
15	2	455
17	3	500
18	3	519
19	3	537
20	3	558
21	3	579
22	3	590
22	4	626
23	3	607
24	4	712
30	4	783
45	6	1114

Vibrational mode assignment of protonated phenylalanine monomer**Table A.2** Vibrational modes assigned to the infrared bands of [Phe+H]⁺.

IR bands [cm ⁻¹]		Assigned vibrational modes
Exp.	Theor.	
1770	1746	$\nu(\text{C}=\text{O})$
1459	1433	$\delta_{\text{scis}}(\text{CH}_2)$ and $\nu(\text{C}=\text{C}) + \delta(\text{C}-\text{H})$ in $-\text{C}_6\text{H}_5$ ring
1141	1419	$\delta_{\text{umb}}(\text{NH}_3^+)$
1415	1384	$\delta_{\text{umb}}(\text{NH}_3^+) + \delta(\text{C}-\text{O}-\text{H})$
1174	1171	$\delta(\text{C}-\text{H}) + \delta(\text{C}-\text{O}-\text{H})$
1153	1158	$\delta(\text{C}-\text{O}-\text{H})$

Appendix B

Side-Chain Monofluorination of Phenylalanine

Experimental collision cross-section ($^{DT}CCS_{He}$) values

Table B.1 Experimentally obtained $^{DT}CCS_{He}$ values of protonated, side-chain monofluorinated Phe clusters where n corresponds to the number of amino acid monomer and z the charge state of the cluster.

$[n(oF\text{-Phe})+zH]^{+z}$			$[n(mF\text{-Phe})+zH]^{+z}$			$[n(pF\text{-Phe})+zH]^{+z}$		
n	z	$^{DT}CCS_{He} [\text{\AA}^2]$	n	z	$^{DT}CCS_{He} [\text{\AA}^2]$	n	z	$^{DT}CCS_{He} [\text{\AA}^2]$
1	1	74	1	1	74	1	1	74
2	1	116	2	1	114	2	1	114
8	2	293	3	1	154	6	1	248
9	2	333	5	1	228	8	2	301
10	2	352	8	2	301	9	2	330
11	2	380	9	2	327	10	2	352
12	2	396	10	2	347	11	2	385
13	2	414	11	2	383	12	2	401
14	2	435	12	2	402	13	2	420
15	3	473	13	2	414	14	2	439
16	3	494	14	2	435	15	2	459
17	3	506	15	2	451	16	2	479
18	3	5245	16	2	471	17	2	493
19	3	538	17	2	496	17	2	478
26	4	717	18	3	522	18	2	510
			19	3	537	19	2	533
			20	3	557	20	2	548
			21	3	574	22	3	604
			22	3	598	23	3	626
			24	3	632	24	3	647
						25	3	660
						26	3	680
						27	3	701
						32	4	827
						34	4	847
						36	4	880

Vibrational mode assignments of protonated, monofluorinated Phe monomer derivatives

Table B.2 Vibrational modes assigned to the infrared bands of [(*o*F-Phe)+H]⁺.

IR bands [cm ⁻¹]		Assigned vibrational modes
Exp.	Theor.	
1774	1748	$\nu(\text{C}=\text{O})$
	1618	$\nu(\text{C}=\text{C})$ in $-\text{C}_6\text{H}_4\text{F}$ ring
	1571	
	1603	$\delta_{\text{scis}}(\text{NH}_3^+)$
	1591	
1471	1467	$\nu(\text{C}=\text{C}) + \delta(\text{C}-\text{H})$ in $-\text{C}_6\text{H}_4\text{F}$ ring
1447	1444	$\delta_{\text{umb}}(\text{NH}_3^+)$
1423	1435	$\delta_{\text{scis}}(\text{CH}_2)$ and $\nu(\text{C}=\text{C}) + \delta(\text{C}-\text{H})$ in $-\text{C}_6\text{H}_4\text{F}$ ring
	1421	
1408	1384	$\delta_{\text{umb}}(\text{NH}_3^+) + \delta(\text{C}-\text{O}-\text{H})$
1215	1197	$\nu(\text{C}-\text{F}) + \nu(\text{C}=\text{C}) + \delta(\text{C}-\text{H})$ in $-\text{C}_6\text{H}_4\text{F}$ ring
1155	1161	$\delta(\text{C}-\text{O}-\text{H})$
1129	1141	$\nu(\text{C}-\text{F}) + \nu(\text{C}=\text{C}) + \delta(\text{C}-\text{H})$ in $-\text{C}_6\text{H}_4\text{F}$ ring
1114	1110	$\delta_{\text{twist}}(\text{NH}_2)$

Table B.3 Vibrational modes assigned to the infrared bands of [(*m*F-Phe)+H]⁺.

Exp.	IR bands [cm ⁻¹]		Assigned vibrational modes
	Exp.	Theor.	
1769		1747	$\nu(\text{C}=\text{O})$
		1602	$\delta_{\text{scis}}(\text{NH}_3^+)$
		1543	
1580		1581	$\nu(\text{C}=\text{C}) + \delta(\text{C}-\text{H})$ in $-\text{C}_6\text{H}_4\text{F}$ ring
1475		1466	$\nu(\text{C}=\text{C}) + \delta(\text{C}-\text{H})$ in $-\text{C}_6\text{H}_4\text{F}$ ring
1453		1433	$\delta_{\text{scis}}(\text{CH}_2)$ and $\nu(\text{C}=\text{C}) + \delta(\text{C}-\text{H})$ in $-\text{C}_6\text{H}_4\text{F}$ ring
1439		1420	$\delta_{\text{umb}}(\text{NH}_3^+)$
1410		1384	$\delta_{\text{umb}}(\text{NH}_3^+) + \delta(\text{C}-\text{O}-\text{H})$
1265		1241	$\nu(\text{C}-\text{F}) + \nu(\text{C}=\text{C}) + \delta(\text{C}-\text{H})$ in $-\text{C}_6\text{H}_4\text{F}$ ring
1163		1186	$\delta(\text{C}-\text{H})$
1150		1159	$\delta(\text{C}-\text{O}-\text{H})$
1133		1126	$\nu(\text{C}-\text{F}) + \nu(\text{C}=\text{C}) + \delta(\text{C}-\text{H})$ in $-\text{C}_6\text{H}_4\text{F}$ ring

Table B.4 Vibrational modes assigned to the infrared bands of [(pF-Phe)+H]⁺.

Exp.	IR bands [cm ⁻¹]		Assigned vibrational modes
	Exp.	Theor.	
1769		1747	$\nu(\text{C}=\text{O})$
1592		1596	$\delta_{\text{scis}}(\text{NH}_2) + \delta(\text{C}-\text{H})$ in $-\text{C}_6\text{H}_4\text{F}$ ring
		1581	$\nu(\text{C}=\text{C})$ in $-\text{C}_6\text{H}_4\text{F}$ ring
		1541	$\delta_{\text{scis}}(\text{NH}_2)$
1505		1490	$\nu(\text{C}-\text{F}) + \nu(\text{C}=\text{C}) + \delta(\text{C}-\text{H})$ in $-\text{C}_6\text{H}_4\text{F}$ ring
1457		1433	$\delta(\text{CH}_2)$
1437		1419	$\delta_{\text{umb}}(\text{NH}_3^+)$
1410		1383	$\delta_{\text{umb}}(\text{NH}_3^+) + \delta(\text{C}-\text{O}-\text{H})$
1256		1228	$\nu(\text{C}-\text{F})$ in $-\text{C}_6\text{H}_4\text{F}$ ring
1155		1158	$\delta(\text{C}-\text{O}-\text{H})$
1116		1145	$\nu(\text{C}-\text{F}) + \nu(\text{C}=\text{C}) + \delta(\text{C}-\text{H})$ in $-\text{C}_6\text{H}_4\text{F}$ ring

Vibrational mode assignments of protonated, monofluorinated Phe homodimer derivatives

Table B.5 Vibrational modes assigned to the infrared bands of $[2(oF\text{-Phe})+H]^+$.

Exp.	IR bands [cm^{-1}]		Assigned vibrational modes
		Theor. (Type A)	
1773		1756	$\nu(\text{C}=\text{O})$
1720		1732	
1604		1609	$\delta_{\text{scis}}(\text{NH}_3^+)$
1578		1597	
1563		1576	$\nu(\text{C}=\text{C})$ in $-\text{C}_6\text{H}_4\text{F}$ ring
1521		1531	$\delta_{\text{umb}}(\text{NH}_3^+)$
1486		1470	$\nu(\text{C}=\text{C}) + \delta(\text{C}-\text{H})$ in $-\text{C}_6\text{H}_4\text{F}$ ring
1457		1434	$\delta_{\text{scis}}(\text{CH}_2)$
1397		1484	$\nu(\text{C}-\text{O}) + \delta(\text{C}-\text{O}-\text{H})$
1352		1313	$\nu(\text{C}-\text{O}) + \delta(\text{C}-\text{O}-\text{H})$
1228		1214	$\nu(\text{C}-\text{F})$ in $-\text{C}_6\text{H}_4\text{F}$ ring
		1203	
1154		1155	$\nu(\text{C}-\text{O}) + \delta(\text{C}-\text{O}-\text{H})$
1097		1101	$\delta_{\text{twist}}(\text{NH}_3^+) + \delta(\text{C}-\text{H})$
		1088	$\nu(\text{C}-\text{F}) + \delta(\text{C}-\text{H})$ in $-\text{C}_6\text{H}_4\text{F}$ ring
1031		1057	$\nu(\text{C}-\text{NH}_2) + \nu(\text{C}-\text{NH}_3^+)$
		1048	

Table B.6 Vibrational modes assigned to the infrared bands of $[2(mF\text{-Phe})+H]^+$.

Exp.	IR bands [cm^{-1}]		Assigned vibrational modes
	Theor. (Type A)		
1775	1757		$\nu(\text{C}=\text{O})$
1724	1735		
1617	1608		$\delta_{\text{scis}}(\text{NH}_3^+)$
1608	1605		$\nu(\text{C}=\text{C})$ in $-\text{C}_6\text{H}_4\text{F}$ ring
1587	1594		$\delta_{\text{scis}}(\text{NH}_2)$
	1585		
	1580		$\nu(\text{C}=\text{C})$ in $-\text{C}_6\text{H}_4\text{F}$ ring
1510	1543		$\delta_{\text{umb}}(\text{NH}_3^+)$
1487	1469		$\nu(\text{C}=\text{C}) + \delta(\text{C}-\text{H})$ in $-\text{C}_6\text{H}_4\text{F}$ ring
1448	1438		$\nu(\text{C}=\text{C}) + \delta(\text{C}-\text{H})$ in $-\text{C}_6\text{H}_4\text{F}$ ring + $\delta_{\text{scis}}(\text{CH}_2)$
	1430		
1404	1384		$\nu(\text{C}-\text{O}) + \delta(\text{C}-\text{O}-\text{H})$
	1377		
1270	1235		$\nu(\text{C}-\text{F})$ in $-\text{C}_6\text{H}_4\text{F}$ ring
1171	1167		$\nu(\text{C}-\text{O}) + \delta(\text{C}-\text{O}-\text{H})$
1151	1155		
1138	1141		
1082	1127		$\nu(\text{C}-\text{F}) + \delta(\text{C}-\text{H})$ in $-\text{C}_6\text{H}_4\text{F}$ ring
	1119		
1042	1060		$\nu(\text{C}-\text{NH}_2)$
	1053		$\nu(\text{C}-\text{NH}_3^+)$
999	1003		$\delta_{\text{wag}}(\text{NH}_2)$

Table B.7 Vibrational modes assigned to the infrared bands of $[2(p\text{F-Phe})+\text{H}]^+$.

Exp.	IR bands [cm^{-1}]		Assigned vibrational modes
	Theor. (Type A)		
1776	1749		$\nu(\text{C}=\text{O})$
1721	1732		
1603	1620		$\delta_{\text{scis}}(\text{NH}_3^+)$
1594	1599		$\nu(\text{C}=\text{C})$ in $-\text{C}_6\text{H}_4\text{F}$ ring
1578	1586		$\delta_{\text{scis}}(\text{NH}_2)$
	1515		$\delta_{\text{umb}}(\text{NH}_3^+)$
1511	1491		$\nu(\text{C}-\text{F}) + \nu(\text{C}=\text{C}) + \delta(\text{C}-\text{H})$ in $-\text{C}_6\text{H}_4\text{F}$ ring
1447	1435		$\delta_{\text{scis}}(\text{CH}_2)$
1401	1387		$\nu(\text{C}-\text{O}) + \delta(\text{C}-\text{O}-\text{H})$
1253	1224		$\nu(\text{C}-\text{F}) + \delta(\text{C}-\text{H})$ in $-\text{C}_6\text{H}_4\text{F}$ ring
	1216		
1161	1161		$\nu(\text{C}-\text{O}) + \delta(\text{C}-\text{O}-\text{H})$
	1135		
1146	1145		$\nu(\text{C}-\text{F}) + \delta(\text{C}-\text{H})$ in $-\text{C}_6\text{H}_4\text{F}$ ring
	1143		
1101	1052		$\nu(\text{C}-\text{NH}_2) + \nu(\text{C}-\text{NH}_3^+)$

Appendix C

Perfluorination of the Phenylalanine Side-Chain

Experimental collision cross-section ($^{DT}CCS_{He}$) values

Table C.1 Experimentally obtained $^{DT}CCS_{He}$ values of protonated F₅-Phe clusters where n corresponds to the number of amino acid monomer and z the charge state of the cluster.

$[n(F_5\text{-Phe}) + zH]^{+z}$		
n	z	$^{DT}CCS_{He} [\text{\AA}^2]$
1	1	81
2	1	129
3	1	168
9	2	335
10	2	357
11	2	385
12	2	407
13	2	431
14	2	455

Vibrational mode assignments of protonated pentafluorophenylalanine monomer

Table C.2 Vibrational modes assigned to the infrared bands of $[(F_5\text{-Phe})+H]^+$.

Exp.	IR bands [cm^{-1}]		Assigned vibrational modes
	Exp.	Theor.	
1772		1748	$\nu(\text{C}=\text{O})$
		1632	$\nu(\text{C}=\text{C})$ in $-\text{C}_6\text{F}_5$ ring
		1600	$\delta_{\text{scis}}(\text{NH}_2)$
		1575	
1506		1496	$\nu(\text{C}=\text{C}) + \nu(\text{C}-\text{F})$ in $-\text{C}_6\text{F}_5$ ring
1498		1480	
1462		1437	$\delta_{\text{umb}}(\text{NH}_3^+)$
1443		1390	$\delta_{\text{umb}}(\text{NH}_3^+) + \delta(\text{C}-\text{O}-\text{H})$
1406		1161	$\delta(\text{C}-\text{O}-\text{H})$
1146		1116	$\nu(\text{C}-\text{F})$ in $-\text{C}_6\text{F}_5$ ring
1130		1085	
1032		1061	$\delta_{\text{twist}}(\text{NH}_2)$

Vibrational mode assignments of protonated pentafluorophenylalanine homodimer
Table C.3 Vibrational modes assigned to the infrared bands of $[2(\text{F}_5\text{-Phe})+\text{H}]^+$.

Exp.	IR bands [cm^{-1}]		Assigned vibrational modes
		Theor. (Type B)	
1782		1749	$\nu(\text{C}=\text{O})$
1728		1677	
1668		1637	$\nu(\text{C}=\text{C})$ in $-\text{C}_6\text{F}_5$ ring
1659		1622	$\delta_{\text{scis}}(\text{NH}_3^+)$
1598		1581	
1647		1612	$\delta_{\text{scis}}(\text{NH}_2)$
1544		1523	$\delta_{\text{umb}}(\text{NH}_3^+)$
1527		1497	$\nu(\text{C}=\text{C}) + \delta(\text{C}-\text{F}) + \delta(\text{C}-\textit{p}\text{F})$ in $-\text{C}_6\text{F}_5$ ring
1510		1484	$\nu(\text{C}=\text{C}) + \delta(\text{C}-\text{F})$ in $-\text{C}_6\text{F}_5$ ring + $\delta_{\text{twist}}(\text{CH}_2)$
		1476	
1424		1431	$\delta_{\text{scis}}(\text{CH}_2)$
1405		1417	$\nu(\text{C}-\text{OH}) + \delta(\text{C}-\text{O}-\text{H})$
1157		1174	
		1110	$\nu(\text{C}-\text{F})$ in $-\text{C}_6\text{F}_5$ ring
1093		1095	$\nu(\text{C}-\text{F})$ in $-\text{C}_6\text{F}_5$ ring + $\delta_{\text{twist}}(\text{NH}_3^+) + \delta_{\text{wag}}(\text{CH}_2)$
		1089	$\nu(\text{C}-\text{F})$ in $-\text{C}_6\text{F}_5$ ring + $\delta_{\text{twist}}(\text{NH}_2) + \delta_{\text{wag}}(\text{CH}_2)$
1051		1079	$\nu(\text{C}-\text{NH}_3^+)$
1038		1074	$\nu(\text{C}-\text{NH}_2)$

Statutory Declaration

by Rayoon Chang, born October 27, 1992 in Uijeongbu, Republic of Korea

I hereby declare that this master thesis entitled “Phenylalanine in the gas phase – the impact of side-chain fluorination” is a result of my personal work and that no other than the indicated aids have been used for the completion of this thesis. Beyond this, I assert that this thesis has not been used to pass any previous examinations.

Berlin, November 05, 2018

Rayoon Chang